Angled spar battery-wing system for large all-electric aircraft

Marek Gryszka[a,*] (Researcher), Saullo G. P. Castro[a] (Supervisor)

[a] Department of Aerospace Structurs & Materials, Faculty of Aerospace Engineering, Delft University of Technology, Kluyverweg 1, 2639HS, Delft, The Netherlands

ARTICLE INFO

Keywords:
all-electric aircraft
finite element analysis
aeroelasticity
wing design
structural design

ABSTRACT

An unconventional structural design is proposed for a battery-housing wing of a large electric aircraft. Locating the batteries in the wing is beneficial for aircraft range, however, it poses a number of additional requirements, with the most constraining being the necessity of regular battery replacement. To enable that, this work proposes using prismatic battery packs and replacing ribs with their truss counterparts and angled spars. This provides an unobstructed path for battery extraction while allowing the wing to remain structurally stable. To size the wingbox, finite element-based linear buckling and stress analyses are performed, and an aeroelastic behaviour estimation method is developed, verified and employed. The resultant wing is fully strength-constrained, 8-13% heavier than the baseline, and capable of satisfying the novel battery-related requirements. A subsequent redesign to address the excessive stiffness and mass is proposed.

1. Introduction

A large battery-electric aircraft E9X has been proposed by Elysian Aircraft [1]. Due to careful requirement selection, as well as novel design choices, such as storing the batteries in the wing, using kerosene as energy reserves for diversion and loiter, and utilising distributed propulsion, the company aims for a range of 800 km, much greater than what was previously deemed achievable with all-electric aircraft [1, 2]. There are, however, numerous new challenges that come with this approach. Among other aspects, storing the batteries in the wings proves to be particularly challenging. First, the logistics of such storage are complex enough to require a battery-wing integrated system design. Second, the presence of the batteries adds a substantial amount of inertia, which might influence which load cases are critical for the wing structural sizing. These two issues were identified in de Vries et al. [1] and referred to as *Challenges 1* and *2*, respectively.

As for the additional requirements posed on the wing by the batteries, they have to be connected to low- and high-voltage circuits, first to power their own power distribution systems and other secondary on-board systems, second to provide the necessary voltage for propulsion. On top of that, a thermal management system is required to keep the batteries and powertrain components within operating temperatures, and a ventilation system is necessary to dispose of fumes in case of a thermal runaway. An example of proposed electric aircraft battery modules, which is taken as reference in this work, is one developed by Electric Power Systems [3]. Another difficulty is that due to battery degradation (and high depth of discharge at which a long-range electric aircraft operates), the batteries have to be replaced multiple times during the life of an airframe.

*Corresponding author

marek@gryszka.pl (M. Gryszka); s.g.p.castro@tudelft.nl (S.G.P. Castro)

www.tudelft.nl/en/staff/s.g.p.castro (S.G.P. Castro)

ORCID(s): 0009-0007-2439-2159 (M. Gryszka); 0000-0001-9711-0991 (S.G.P. Castro)

The battery replacement is a non-trivial task, as the batteries, unlike fuel, are solid objects, and there must exist an unblocked path to remove them and insert new ones. This contrasts with the structure of a conventional wing, which is a box beam, taking its stiffness from sheet metal placed along all three dimensions in the form of skin, spars, and ribs. The skin is the main bending-carrying element, the spars are necessary to form a closed cross-section for carrying torsion, and the ribs address buckling and flattening of the cross-section under bending, known as the Brazier effect [4, p.596]. To extract batteries, one of the wingbox components would have to be opened, potentially compromising the structural integrity of the wing, or a completely different design philosophy would have to be adapted that achieves a similar level of strength and stiffness without placing material along a particular direction.

As for *Challenge 2*, while the additional mass present in the wing provides a significant amount of bending relief, the addition of inertia worsens the landing loads, as well as impacts the aeroelastic performance of the structure [1]. As such, it is necessary to include these load cases in the preliminary design of the wing to avoid an overestimation of the structural performance.

A potential solution to *Challenge 1* has been outlined by Kemperink [5], following the approach of opening a part of the wingbox. The ribs were selected for opening, as they are loaded strictly in-plane, so provided that the shear and normal loads remained transferable, the structure remained stable. Then, batteries were moved spanwise along a pair of worm-gear rails to be extracted through a limited number of opening points, similar to a landing gear opening in conventional aircraft. This strategy has numerous benefits, such as staying relatively close to a conventional aircraft structure and utilising standard-size rectangular battery packs. At the same time, the design of such openable ribs is yet to be fully examined, and this solution places significant constraints on the wing geometry, where the two rails have to remain parallel, thus forcing the wing to remain rectangular with no taper ratios. This constraint has a negative impact on the wing aerodynamic performance. Last, but not least, opening the reinforced ribs to which the motors and the landing gear are mounted might prove to be challenging, if not impossible, heavily constraining the location of extraction points along the wing.

As an alternative to opening a part of the conventional wing structure, one can aim for a structural layout in which openings naturally exist, such as a truss. A design of a truss-based wing structure has already been proposed and studied for the occurrence of flutter [6]. Originally, the key benefit of such a structure was identified as modularity, which allows for cheaper and simpler manufacturing and maintenance. What is of more interest in the approach for *Challenge I* is the ability to extract battery packs through the triangular empty spaces present in the structure.The truss structure comes with its own set of challenges: the stability of the skin, which is no longer continuously supported by the spars and the ribs, and the triangularity of the openings, which necessitates either a custom battery pack design or significant space losses if conventional cuboidal battery packs are used. That being said, the risks and opportunities associated with this solution are substantially different from those of opening a part of the wingbox. As such, exploring structures with naturally occurring openings, such as trusses, might allow for diversifying the solutions to battery replacement available.

The present study conducts a preliminary design of a wing structure for the aircraft proposed by Elysian, subject to landing loads and aeroelastic constraints, such that the batteries present in the wing can be removed without large-scale opening or disassembly of the wing's primary structures. As a secondary objective, this is to be done while preserving the original wing geometry. The focus is placed less on obtaining a fully optimised design, but more on design space exploration and assessing whether *Challenges I* and *II* can be viably addressed with the adopted approach.

During the development of the present work, a second iteration on the E9X concept was published [7]. Also, Wang et al. [8] compared different solutions to *Challenge II*, but did not consider battery replacement. In this study, the first-iteration wing geometry of E9X is used [1], but qualitative remarks from the second-iteration results are considered when possible.

2. Method

The methodology is presented as follows: first, the requirements imposed by the presence of the batteries and the load cases which the wing must withstand are outlined in subsection 2.1, then an implementation of the angled spar idea capable of meeting the requirements is presented and parametrised in subsection 2.2. Afterwards, a finite element model of the wing is defined in subsection 2.3 and overlaid with a vortex lattice mesh. subsection 2.4 contains an explanation on how simulation results are processed to assess whether structural failure occurs or not. Finally, subsection 2.5 describes the optimisation procedure used to find values for element thicknesses.

2.1. Requirement Analysis

The wing is required to provide a safe and accessible housing for the batteries, as well as withstand the loads applied to it during all phases of aircraft operation. In this subsection, the battery requirements are given together with the load cases considered, to serve as a quantifiable statement of the design problem.

2.1.1. The Battery Requirements

- **RB1:** the wing shall house the required mass of batteries of 35 tons, under the assumptions about battery density made during the original aircraft design [1].
- **RB2:** the batteries shall be connected to the piping of the thermal management system, low voltage wiring for the secondary subsystems, and to high voltage propulsion cables. All those connections shall be undone and re-established during the battery replacement procedure.
- **RB3:** Each battery shall have its dedicated ventilation pipe not shared directly with other batteries [3].
- **RB4:** any battery pack shall not bear any loads other that its own inertial load.
- **RB5:** the battery replacement procedure shall not involve disassembly of aircraft primary structures.
- **RB6:** the batteries shall be fully replaceable in no more than 24 hours.
- **RB7:** the batteries need to provide a low-voltage current to power the on-board systems and their own thermal management, as well as 1kV current to power the motors.
- **RB8:** all maintenance access holes shall be located on the lower skin of the wing.

Regarding **RB1** the exact battery mass, together with the Class II weight breakdown of the original design, have been provided by Elysian Aircraft for this study and are used for obtaining the final results, however they cannot be published. Consequently, the mass of the wingbox designed in this study is provided in relative terms only. The purpose of **RB2** and **RB3** is to ensure the batteries are both fully operational and replaceable in the designs proposed herein. While the battery packs themselves, in order to be certified, must suppress the propagation of thermal runaway on a cell-to-cell level [9], it is vital that the system does not increase the probability of a battery failure, as it would have significant reliability consequences. As such, **RB4** is established. **RB5** is included for solutions to stay relevant to the research question. **RB6** ensures the replacement can be conducted during the scheduled maintenance, as envisioned during the E9X design [1]. **RB7** is imposed, as outlined by de Vries et al. [7], DC-DC converters negatively influence the mass of the high-voltage subsystem. The value of 1 kV is selected as

Table 1
Load cases considered for the preliminary design.

ID.	Description	Load Factor (Lift)	Load Factor (Landing Gear)	Thrust	Altitude	Airspeed
LC0	pull-up maneuver	2.5	0	112.8 kN	0	90 m/s
LC1	pull-down maneuver	-1	0	32.4 kN	7000 m	187 m/s
LC2	maximum speed	1	0	37.8 kN	0	215 m/s
LC3	landing	1	1.5	0	0	74 m/s

being in a lower range of voltages considered for powertrain design by Ebersberger et al. [10], at the same time being reported as a soft upper bound by Alexander et al. [11] due to a phenomenon of corona discharge. Finally, **RB8** is imposed to avoid complications in maintenance logistics.

2.1.2. Load Cases Considered

The considered wing has originally been sized considering a 2.5g pull-up manoeuvre by de Vries et al. [1]. According to the authors, the landing or aeroelastic loads might be more constraining compared to conventional aircraft, due to a large amount of weight in the wings (*Challenge 2*). Thus, in the present study, a landing scenario is added next to the original load case. The landing gear load factor (so the ratio of reaction force to weight) is assumed to equal 1.5 for two-point landing (so 3/4 of aircraft weight on each gear), as used by Naghshineh-Pour [12]. Single-point landing is not considered, as it is challenging to model quasi-statically: for such cases, the impact is immediately followed by aircraft rotation. To ensure the structure can bear negative load factors, it is necessary to add a -1 load factor load case is also included. Last but not least, the case of steady flight at the maximum speed must be added. For this load case, the presence of flutter is examined. It would not be suitable to check for flutter at the other load cases, as they are almost instantaneous: oscillations would not have time to reach a steady state during landing impact or pull-up. The maximum speed for flutter assessment is determined according to the rules of certification tests published by EASA [13, p.360]. In the absence of a full aircraft flight envelope, the cruise speed multiplied by a factor of 1.15 at sea level is taken as constraining. An overview of the load cases is presented in Table 1.

The thrust values in Table 1 are the total for all engines combined and are based on power-loading values from the original design, corresponding to take-off, cruise, maximum thrust, and landing (zero thrust) for the four load cases, respectively [1].

2.1.3. Failure Modes

The structure cannot exhibit aeroelastic instability up to the maximum speed and has to be verified against exceeding the allowable stresses or buckling for the load cases in Table 1. As the load cases are expressed in terms of limit loads, sufficient safety factors must be used to ensure compliance with the 1.5 times higher ultimate loads.

For stresses, there must be no yielding at the limit load and no fracture at the ultimate load. This means that, depending on the material yield-to-ultimate strength ratio, either the yield strength or the ultimate strength divided by 1.5 is considered the allowable stress.

For buckling, due to the preliminary nature of the study, a conservative approach is applied, not allowing for buckling until the ultimate load. This means that the load multiplier to be used as a threshold for the linear buckling analysis of the limit-load load cases is 1.5.

For **LC2**, the load factor is significantly lower than that of **LC0**. As such, in terms of stresses and buckling, **LC2** is in all likelihood less constraining than the pull-up manoeuvre and thus not evaluated. Instead, an aerodynamic matrix is constructed and the onset of aeroelastic effects, such as flutter or divergence, is examined for this load case, following the procedure in subsubsection 2.4.4. In the absence of damping data, aeroelastic instability is indicated by a coalescence of natural frequencies, as used by Guimarães et al. [14].

2.2. Conceptual Design and Parametrisation

Based on the requirements of subsection 2.1, the conceptual design starts with a qualitative proposal of the solution adopted in this work. Following that, a parametrisation of the design is established. This allows verification of the available battery volume and serves as a basis for further design steps.

2.2.1. The angled spar concept

Following Kemperink [5], the batteries are extracted by moving them spanwise and removing them through a single cutout at the wing root, or if that is impossible due to obstruction provided by the motors, through multiple cutouts near the motor locations. The reason for that is that the role of ribs (preventing buckling, serving as attachment of equipment to the wing and preserving the cross-section shape [15, p. 644]) is considered secondary to the role of skins and spars, which carry the bending and torsional loads the wing experiences.

Instead of removing ribs completely or making them openable, it is proposed to replace them with a truss counterpart, so that batteries can be slid on lead screw rails through the empty space in the truss, satisfying **RB5**. To compensate for the weakening of the ribs and provide supports to the battery rails, additional spars are placed at an angle matching that of the truss rib members. The outline of the design is presented in Figure 1.

The proposed battery packs are made of close-packed hexagonal (CPH) cylindrical cells, resulting in a triangular or trapezoidal cross-section with 60° angles, which fits through a truss rib with members at this angle. Selecting this cross-section is a compromise between battery pack and structural design. CPH enables compact and regular internal layout for the battery packs, whereas the 60° truss rib member angle leads to a relatively dense network of the angled spars supporting the skin. At the same time, off-the-shelf rectangular battery modules [3] cannot be used to create the packs and the wingbox dimensions become constrained by having to accommodate a pattern of sheets at pre-defined angles.

As the ribs are weakened, buckling resistance becomes a concern. Also, the proposed battery packing pattern results in a multi-cell wingbox, with not all cells directly connected to the leading or the trailing edge, which might pose a challenge in satisfying the battery requirements. Those issues are addressed by making the skins and spars sandwich panels instead of stiffened webs. The sandwich panels provide uniform buckling and local bending resistance, while wires and thermal management pipes can be led through their core to the interior battery packs, as shown in Figure 1. This, however, requires the skin sandwich panels to be sufficiently thick. A common problem with sandwich panels is moisture ingression [16], but it can be addressed by creating cutouts in the interior skin of the panel, as proposed by Okamoto et al. [17].

The panels and the lead screw rails are split into segments connected via rivets or bolts and heated inserts. This is heavier than bonding, but allows for local component replacement, which may be required in case of local failure of the wires inside the sandwich panels. Double-countersinking of rivets is used to avoid interfering with battery space, and double-lap joints are used for the skin to preserve a smooth outer surface.

Due to concentrated inertial loads from batteries and a large number of holes and cutouts, aluminium is considered the primary skin material for the sandwich panels. When applicable, glass fibre-reinforced polymer (GFRP) skins can be used for their insulating properties. As GFRP does not accelerate aluminium corrosion [18], blending the two materials is considered acceptable.

Access holes, connections between the battery packs and thermal management pipes, as well as exhaust pipes for thermal runaway ejecta are all located on the lower side of the wing. This is to satisfy **RB8**. For batteries whose rails are attached to the lower skin, this creates a space-constrained situation. To resolve that, it is proposed to place different connections at different spanwise positions along the pack. The top skin is dedicated to electrical wiring, as electricity through conduction does not require a fixed connection, only contact. Overall, the setup allows for satisfying **RB2** and **RB3**

The sizing of the rail system is considered out of scope for this study. Instead, an effective rail diameter of 30 mm

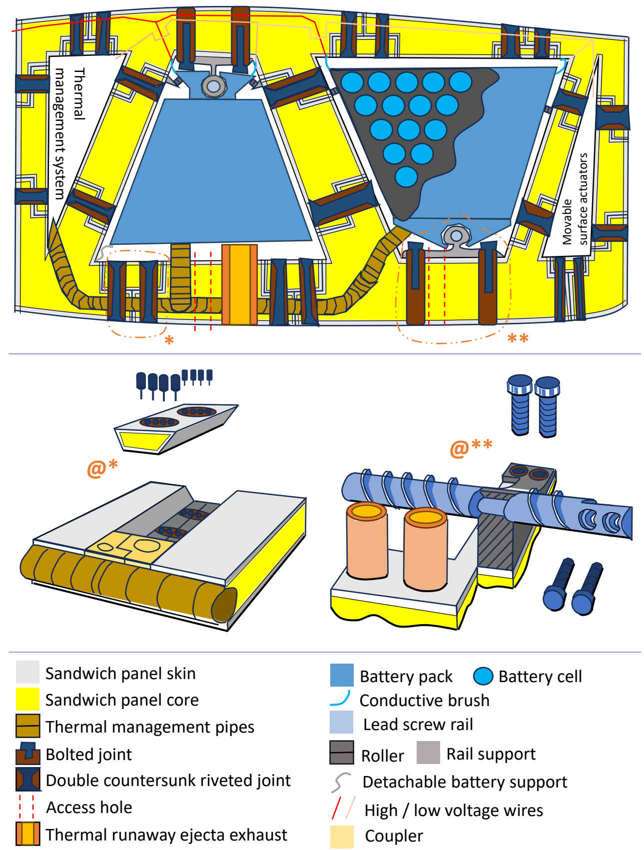

Figure 1: Sketch of the angled spar wingbox, including connections between sandwich panels and rails as well as the required battery interfaces.

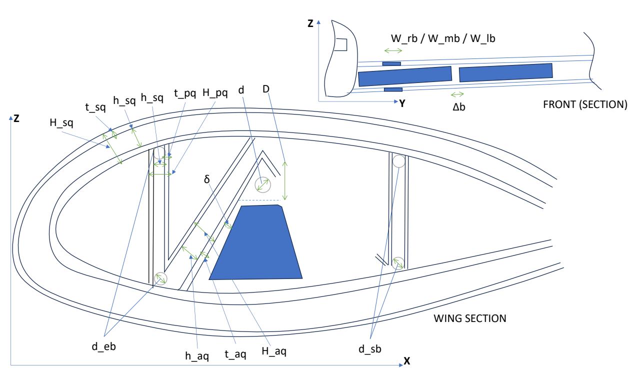

Figure 2: Definition of parameters of the *angled spars* design.

is assumed for structural analysis, and the impact of this parameter is later assessed by means of a sensitivity study.

2.2.2. *Parametrisation*

To parametrise the above conceptual design, one needs to address the space taken by the spars, the rails and the skin, as well as the sheet thicknesses of specific elements. The former are concerned with the space available inside the wing and, in principle, could be as large as the battery pack allows. As such, they are to be treated as hyperparameters. The latter are design variables to be determined during optimisation. The set of parameters used is defined in Figure 2.

The total thickness of elements is denoted as H, the sheet thicknesses as t, the core thicknesses h. The subscripts for the skin are $_{sq}$, for the vertical spars $_{pq}$, and for the angled spar $_{aq}$. On top of that, there is a hyperparameter δ that denotes the tolerance spacing between a battery and a sandwich sheet. Parameters concerned with rails are d, which is used as the rail diameter for structural calculations and D, the battery triangle height taken by the entire rail system. The ribs are modelled as an assembly of rectangular beams of height equal to local H and width being an optimizable parameter equal for all ribs of the same type. There are W_r, W_m, and W_{LG}, corresponding to regular rib, reinforced rib at the motor location, and reinforced rib at the landing gear location, respectively. The spacing between batteries in the spanwise direction Δb is treated as a hyperparameter. d_e and d_s are diameters of reinforcements along the fore and aft corners of the wingbox, treated as design variables.

H parameters are not meant to be constant along the span. That would leave little to no space for the batteries near the wing tip or not enough stiffness to counter buckling at the wing root. Instead, ratios of H over local chord length H/c are set as constant, as well as ratios of sheet thickness over total thickness $2t/H$. Different values of $2t/H$ are used inboard and outboard of the second engine from the fuselage. The inboard ratios have capital subscripts, i.e. $_{Sq}$ instead of $_{sq}$. Overall, there are eleven free variables $\mathbf{v}_f$ and seven hyperparameters $\mathbf{v}_h$:

$$\mathbf{v}_f = \begin{bmatrix} \left(\frac{2t}{H}\right)_{Sq} \\ \left(\frac{2t}{H}\right)_{sq} \\ \left(\frac{2t}{H}\right)_{Pq} \\ \left(\frac{2t}{H}\right)_{pq} \\ \left(\frac{2t}{H}\right)_{Aq} \\ \left(\frac{2t}{H}\right)_{aq} \\ d_s \\ d_e \\ W_{bb} \\ W_{mb} \\ W_{lb} \end{bmatrix}; \qquad \mathbf{v}_h = \begin{bmatrix} \left(\frac{H}{c}\right)_{sq} \\ \left(\frac{H}{c}\right)_{pq} \\ \left(\frac{H}{c}\right)_{aq} \\ D \\ d \\ \delta \\ \Delta b \end{bmatrix} \tag{1}$$

The panel skin thickness ratios are bound between 0.03 and 0.3, the rib widths are between 3 and 30 mm, and the spar cap diameters are between 4 and 20 mm. This is to ensure the components remain consistent with their assumptions that sandwich panels must have sufficient space in the core to pass wires through, while ribs and corner reinforcement, modelled as beams, must remain slender.

2.2.3. Battery placement

The angled spar-battery pattern needs to fit between the leading and trailing edge spars at the wing root. The vertical spars are located at 0.1 and as close to 0.65 of the chord

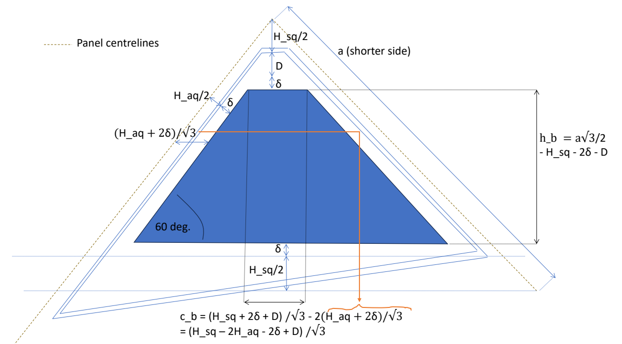

Figure 3: Derivation of the cross-section area available for batteries.

as possible (due to angled spars being at $\pm$ 60° angles, it may not be possible to terminate the spar-battery pattern at 0.65 of the chord exactly). This follows the spar locations provided by Elysian aircraft. The root and tip thickness-to-chord ratios have also been provided by Elysian Aircraft as 0.19 and 0.10, respectively, while other airfoil parameters remain classified. As such, this study uses NACA 2419 and NACA 2410 cross-sections. The root thickness to chord may be adjusted if it is shown that a slightly larger or smaller value accommodates the angled spars significantly better.

Each battery is placed between two ribs of the wing, as the rib truss is expected to provide support for the point load at the battery connection points. The cutout in the outboard rib is the driving factor for the battery size. Figure 3 defines h_b and c_b from which the cross-section area of a battery pack can be found as:

$$A_b = h_b \left(c_b + h_b/\sqrt{3} \right) \tag{2}$$

From that, the battery pack volume can be determined by multiplying A_b with the distance between the ribs less Δb. This derivation assumes $H_{sq} \geq 2H_{as}$, which, given the load-bearing and wire-hosting nature of the skin panels. is expected.

The minimum size required for the battery pack to provide the required 1 kV voltage is found by examining the case of INR21700-40T [19] cells connected in series with a nominal voltage of 3.6 V and a mass of 0.070 kg. Following de Vries et al. [1], it is assumed that end-of-life usable cell mass is 65% of total battery pack mass. This yields a minimum battery pack mass of approximately 30 kg.

2.3. Finite Element and Aerodynamic Models

To assess whether the proposed structure meets the strength, buckling and aeroelasticity requirements, a finite element model implemented using `pyfe3d` version 0.7.0 [20] (subsubsection 2.3.1) and a Vortex Lattice Model implemented using `aerosandbox` [21, 22] (subsubsection 2.3.4) were created. The combination of these two allowed for obtaining aerodynamic loads, structural deformations, and the aerodynamic matrix for the aeroelastic load case. The aerodynamic loads were transferred to the finite element mesh using radial basis interpolation in subsubsection 2.3.5.

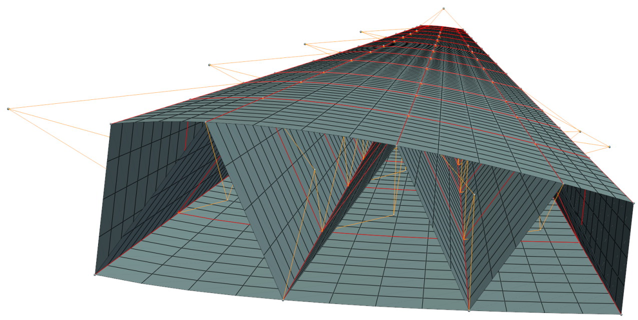

Figure 4: An overview of the structural mesh for $N = 5$.

2.3.1. Finite Element Definition and Mesh

The finite element mesh is constructed using `Quad4R` and `BeamC` elements from `pyfe3d`. First, the skins and spars are meshed so that there are nodes on every rib spanwise position and at every rail or corner reinforcement chordwise position. This creates joint nodes shared by both rails or spanwise reinforcement with ribs. To those nodes, equipment (the batteries, leading- and trailing-edge subsystems, engines, folding wing tip and the landing gear) is attached. Intermediate nodes are created uniformly, so that resultant quadrangular elements are as close to square as possible. A meshing parameter N is used to represent the number of intermediate nodes between two neighbouring chordwise rail positions on the same side (top or bottom) of the wing. Rails, corner reinforcements and truss ribs are modelled as beam elements sharing nodes with the quadrangular elements at the spanwise/chordwise location of the rail/reinforcement/rib. An overview of the mesh is presented in Figure 4.

Attaching the equipment to joint nodes, while consistent with its requirements (for example, to avoid battery bending, they need to be attached to the rails at only two points, as noted by Kemperink [5]), causes stress singularities to occur. As such, the locations around the joints are excluded from the stress recovery, and the effect of point loads is to be determined analytically.

The equipment itself is modelled as point masses and attached via a statically determinate combination of axial springs, which prevents the equipment from bearing the loads from the surrounding structure (as the loads in the springs can be determined from the loads on the equipment solely), thus satisfying **RB4**.

The quadrangular elements representing sandwich panels are modelled using first-order shear deformation theory [20] with three layers representing two sheets and the core. `pyfe3d` automatically computes the shear correction factor, and this automatic result was used for the element.

The truss rib beam elements are modelled using a filled rectangular cross-section beam with height equal to local H and width equal to the respective W parameter. A vector oriented in the direction of the dihedral of the aircraft wing is used to specify the sideways direction for the element. The rail beams and corner reinforcements are modelled as filled circular beams of cross-section diameter equal to d, d_e or d_s. The transverse shear correction factors are obtained using Timoshenko's approach [23].

Table 2
Properties of materials used for the finite element model.

Property	Aluminium-2024-T81 [27]	Sandwich Core
E-modulus	72.4 GPa	586.44 MPa
Poisson ratio	0.33	0.275 [28]
Allowable stress	323.33 MPa	3.645 MPa
Density	2780 kg/m^3	250.2 kg/m^3

The material properties used are presented in Table 2. The sandwich panel skins and beam elements are considered to be made of Aluminium-2024-T81. For this material, the yield and ultimate strength are close together (450 MPa and 485 MPa). As such, the stresses at limit loads are kept significantly below the material's yield strength to prevent fracture under ultimate load, when the ultimate strength should be optimally exploited. Because of that, the ultimate strength divided by 1.5 is used as the maximum allowable stress under limit loads.

The sandwich core is assumed to be an aluminium foam, chosen instead of honeycomb due to the latter being challenging to machine [24] and non-uniform. This would have caused difficulties when creating the cutouts and wire channels in the core. The density, stiffness and strength of the foam are obtained by applying the Gibson and Ashby model [25, 26] with Aluminium-2024-T81 as the base material for the foam. The initial guess for the foam density is one that causes the foam and aluminium to yield at the same strain:

$$\sigma_{y_{al}}/E_{al} = \sigma_{y_{foam}}/E_{foam} => E_{foam}/E_{al} = \sigma_{y_{foam}}/\sigma_{y_{al}}$$

$$\left(\frac{\rho_{foam}}{\rho_{al}}\right)^2 = 0.3\left(\frac{\rho_{foam}}{\rho_{al}}\right)^{1.5} => \frac{\rho_{foam}}{\rho_{al}} = 0.09 \quad (3)$$

The finite element model is created from the end of the fuselage to the hinge line of the folding wingtip only. The wing tip is considered as added inertia, while the structural design of the fuselage-wing intersection is considered out of scope for this study, and the wing is assumed to be clamped at the fuselage boundary.

The static solution, that is, obtaining the model displacements for a given load case, requires solving a sparse system of linear equations $\mathbf{K_{C0_{uu}}u_u} = \mathbf{f_u}$, where $\mathbf{u}$ is the displacement vector, $\mathbf{K_{C0}}$ is the stiffness matrix, and $\mathbf{f}$ is the load vector, while the subscripts $_\mathbf{u}$ and $_\mathbf{uu}$ denote the application of boundary conditions by removing the affected degrees of freedom from the linear system. In this study, the system is solved using `PyPardiso` [29].

2.3.2. Resolving the stress singularities

The point loads at the equipment attachments create stress singularities. In reality, equipment supports have a nonzero size, so their loading would spread over a predetermined area in the structure. The goal of this subsection is to size those supports analytically and determine the mass added by the presence of the joint. For stress recovery, the area inside and around the joint is excluded, and the mass penalty found in this section is applied instead. The area excluded and accounted for by the local analysis must be such that the effect of local geometry is still visible in the global stress recovery, but without the peak stress coming from the singularity [30]. This may require iteratively conducting the convergence study described in subsubsection 2.4.5 to determine suitable sizes for the excluded areas.

Given the way the equipment is attached, only point forces, not moments, are expected at the joints. It is assumed that the attachment is through high-strength bolts as given by the MIL-B-6812E standard [31]. As per Zhou et al. [32], the joint failure modes considered are bearing and fastener failure and the point force is considered to be spread evenly between the joints. Other failure modes, such as sheet tearing, are accounted for by abiding by the minimum spacing guidelines included in Zhou et al. [32]. Inverting the provided equations, one can obtain the minimum number of fasteners in a joint n_j:

$$n_j = \operatorname{ceil} \max \left(\frac{\mathrm{SF}V}{\sigma_b d_f t_{sh}};\ \mathrm{SF}\sqrt{\frac{V^2}{V_{\max}^2} + \frac{N^2}{N_{\max}^2}} \right) \quad (4)$$

where SF is a safety factor of 1.5 added because limit loads are simulated; σ_b, d_f, t_{sh}, $V_{\max}$ and $N_{\max}$ are respectively the sheet bearing strength, fastener diameter, sheet thickness, allowable shear per fastener, and allowable normal load per fastener. The sheets are assumed to be made of Aluminium-2024-T81, with a bearing strength of 441 MPa [27], and their thickness is determined for each joint individually so that the bearing is not constraining even if the joint sees pure shear. The V and N are the shear and normal loads applied to the joint. The joints are modelled as attached to the skin panels via heated inserts, similarly to the rails. As such, the load in the z-axis is interpreted as N, while the load in the remaining axes contributes to V. Due to the way the equipment is mounted in the model, the motor, wing tip, battery and landing gear joints are separate. Thus, there is a clear driving load case for the sizing of each joint, from which V and N can be deduced.

Given the limited space between the corners of the angled spars and the rails running through the middle of those corners, symmetric joints with two bolts in a row are adapted. The number of fasteners is rounded up to obtain an integer number of bolt rows. The sheet is sized based on the minimum bolt spacing. For each joint, all combinations of row number and fastener type are sized, and the one with the smallest longer dimension of the sheet is selected. The mass of the joint is then the sum of the masses of the sheet, fasteners (assumed to be made of steel with density 8000 kg/m^3 [33]) and the heated inserts. The latter is obtained by modelling the heated insert as a tube and interpolating between the provided heated insert's inner diameters [34].

2.3.3. Non-aerodynamic loads

Next to the aerodynamic load, the structure is subjected to thrust, inertial loads, and, for **LC3**, landing gear reaction force.

The inertial loads can be obtained by multiplying the mass matrix by a vector containing, for each degree of freedom, the value of non-inertial frame acceleration, which is the gravitational acceleration vector minus the acceleration of the system as would be seen in an inertial reference frame. This is to model the effect of the pseudo-force that the system feels in its own non-inertial frame.

The landing load is spread between the two point-mass nodes at the two stations of the landing gear ribs. The rationale behind splitting the landing gear into two point masses is to allow for a symmetric, yet statically determinate mounting of the landing gear to the two ribs. As **LC3** describes symmetric landing, 0.75 of the aircraft's weight is applied to each landing gear, which means 0.375 of the aircraft's weight is applied to each landing gear node.

Since the wing is at a nonzero angle of attack, the acceleration and the landing load vectors are not simply zero except at the third degree of freedom of each node. Instead, they have to be rotated in the zx plane to account for the structure being positioned at an angle, and gravity still being applied downwards.

The thrust is aligned with the body reference frame of the aircraft and, as such, does not need to be rotated. It is assumed to be directed exactly towards the negative x of the model reference frame. Half of the total thrust is spread evenly across all modelled engine point masses.

2.3.4. Aerodynamic Model

The Vortex Lattice Method (VLM) of the `aerosandbox` library is used to obtain the aerodynamic loads. An entire span of the wing is meshed, with airfoil stations uniformly spaced from the wing root to the hinge line and an additional station at the wing tip. This allows for including the load at the wing tip when obtaining the aerodynamic loads for static analysis, while excluding the wing tip from aeroelastic analysis. The wing tip is excluded, as its aeroelastic stability is tied to its detailed design, including the effects of the folding mechanism. Those factors are beyond the scope of this study.

Another noteworthy aspect of the aerodynamic model is that some load cases, especially the 2.5g pull-up manoeuvre (**LC1**), involve high values of lift that are not obtainable with a clean wing. Since modelling high-lift devices is a substantial difficulty beyond the scope of this research, it was decided to obtain aerodynamic loads for the clean wing at an angle of attack corresponding to each load case and scale the result to match the load factor.

The selection of model parameters, such as spanwise and chordwise resolution, as well as the number of stations along the wing at which the airfoil is defined, had to be confirmed by a convergence study.

A Prandtl-Glauert correction [35, p.726] is used on top of VLM results to account for compressibility. Due to the linearity of the correction, it can be applied directly to the obtained aerodynamic forces, with no need to evaluate the pressure coefficient distribution.

2.3.5. Interpolation between the Aerodynamic and Structural Meshes

To apply the aerodynamic load to the structural mesh, one can use a data structure that finds a specified number of nearest neighbouring nodes and the distance to them, such as `scipy.spatial.cKDTree` [36, 37]. Based on information provided by the data structure, a radial basis interpolation with the basis function of $1/\text{distance}^2$ is conducted. One can obtain the weights from each point on the aerodynamic mesh to a number of points on the structural mesh, as:

$$w_{fem<-aero}[i,j] = \frac{1/\text{distance}^2_{i,\,j}}{\sum_{k=1}^{n_{points}} 1/\text{distance}^2_{k,\,j}} \tag{5}$$

where n_{points} is the number of finite element nodes considered by the `KDTree` algorithm, for each vortex centre of the aerodynamic mesh. As aerodynamic load is transferred to the translational degrees of freedom of the load vector of the finite element model, this weight needs to be added to three entries in the global weight matrix corresponding to the first three degrees of freedom of the target node. A weight matrix obtained this way can multiply the vector of aerodynamic forces per vortex lattice panel to obtain the aerodynamic force vector applied to the finite element model.

As the number of structural model nodes increases approximately with $O(N^2)$, n_{points} needs to be increased quadratically as well. This is to prevent the load from being spread over an ever-decreasing area of the structural mesh, which would have caused additional stress singularities.

2.4. Post-processing and Failure Evaluation

For each of the considered load cases, one has to verify whether the values of the element stresses have not surpassed an allowable value and examine the occurrence of buckling. Additionally, for **LC2**, it is necessary to perform a flutter analysis. This subsection presents details of those calculations and specifies how failure is determined for each of the failure modes.

2.4.1. Maximum stresses in beam elements

The consistent Timoshenko beam elements implemented in `pyfe3d.BeamC` follow a formulation by Luo [38]. One can use the following formulae from his work to obtain strains at any point of the cross-section of the Timoshenko beam:

$$\begin{cases} \bar{\varepsilon} &= u' \\ \bar{\kappa}_y &= -\theta' \\ \bar{\kappa}_z &= \psi' \\ \gamma_y &= v' - \theta \\ \gamma_z &= w' + \psi \\ \bar{\kappa}_x &= \varphi' \end{cases} ; \begin{cases} \epsilon_{xx} &= \bar{\varepsilon} + \bar{\kappa}_y\, y + \bar{\kappa}_z\, z \\ \epsilon_{xy} &= \gamma_y - \bar{\kappa}_x\, z \\ \epsilon_{xz} &= \gamma_z + \bar{\kappa}_x\, y \end{cases} \tag{6}$$

where $'$ denotes a derivative with respect to position along the length of the beam, and $u, v, w, \phi, \theta, \psi$ are displacements in the six degrees of freedom `pyfe3d` considers, in the local coordinates of the beam element. For each beam in the mesh, those derivatives can be obtained using a finite difference method:

$$u' = \frac{u_2 - u_1}{x_{e2} - x_{e1}} \tag{7}$$

where u_2 and u_1 are displacements in local element lengthwise coordinate x_e at the two nodes of the beam element, and x_{e1} and x_{e2} are values of element x_e at those nodes. If used to estimate the derivative at half of the beam length, the scheme becomes a central difference one. As such, the strains are interpreted as values of strains at the half-length point of each beam element.

From these three strains, normal and shear stresses can be computed by multiplying by the respective modulus, and then, the von Mises failure criterion can be evaluated [39]:

$$\sigma_{\text{v}}^2 = \frac{(\sigma_{11}-\sigma_{22})^2 + (\sigma_{11}-\sigma_{33})^2 + (\sigma_{22}-\sigma_{33})^2}{2} + 3(\sigma_{12}^2 + \sigma_{13}^2 + \sigma_{23}^2) \tag{8}$$

where σ_{ab} denote shear and normal stresses in an arbitrary coordinate system. For beams, this equation further simplifies to:

$$\sigma_v = \sqrt{\sigma_{xx}^2 + 3(\tau_{xz}^2 + \tau_{xy}^2)} \tag{9}$$

where σ_{xx} is the normal stress, and τ_{xz} and τ_{xy} are the two transverse shear stresses.

The remaining question is at which points in the cross-section the von Mises stress should be evaluated. In Appendix A, it is shown that the most constraining von Mises stress must occur at the cross-section boundary, and for the rectangular beam specifically, at one of the corners. For the circular cross-section, the constraining point must be found through brute force by evaluating the von Mises stress at 16 points around the cross-section. With normal and shear stresses varying linearly across the cross section in the Timoshenko model, this corresponds to under-predicting particular stresses by up to 2%. This is for the worst-case scenario when the constraining point lies the furthest (11.25°) away from any evaluation point.

2.4.2. Maximum stress in sandwich panels

The spar and skins are modelled as a sandwich panel, with isotropic skins and cores. The `Quad4R` plate elements used to model them in `pyfe3d` implement Mindlin theory [40]. The theory assumes that the in-plane strains vary linearly along the thickness of the plate, while transverse shear strains are constant along the thickness. Following the `pyfe3d` implementation, the strains at the centre of the `Quad4R` element are calculated in the element coordinate system. Combining this with the material properties of the sandwich components, one can compute normal and shear stresses at various locations along the sandwich thickness and use the corresponding failure criteria per component of the sandwich.

To begin with, at every coordinate along thickness z, normal strains are linear functions of z with the slope dictated by curvatures and average values dictated by average strains. At the same time, Poisson's ratio ν applies:

$$\begin{cases} \kappa_{xx} z + \epsilon_{xx} = \frac{\sigma_{xx}}{E(z)} - \frac{\nu(z)\sigma_{yy}}{E(z)} \\ \kappa_{yy} z + \epsilon_{yy} = \frac{\sigma_{yy}}{E(z)} - \frac{\nu(z)\sigma_{xxy}}{E(z)} \end{cases} \tag{10}$$

The material properties are denoted as a function of z because along the coordinate, one is met with different layers of the laminate, having different properties. Similarly, for in-plane shear:

$$\kappa_{xy} z + \gamma_{xy} = \frac{\tau_{xy}}{G(z)} \tag{11}$$

where G is the transverse shear modulus without the shear correction factor, for the assumed materials equal to $\frac{E}{2(1+\nu)}$ [41, p.126]. The transverse plane shear strains is equal to $\tau_{yz}/(\kappa G)$ and $\tau_{xz}/(\kappa G)$, with κ being the shear correction factor.

In that setting, the most constraining stresses occur at the maximum or minimum value of z for both the core and the sheets. The issue is that while one can use von Mises criterion again to evaluate sheet failure, the core material is porous. Hence, this failure criterion cannot be applied. Instead, one needs to use the failure criterion from Gioux et al. [42]. To evaluate it, one must first compute the principal stresses (eigenvalues of the stress tensor, computed using `scipy.eigh`) and the standard von Mises stress (Equation 8). Then, one needs to compute the *mean stress* σ_m as average of principal stresses and a correction factor α for Poisson's ratio ν:

$$\alpha = 3 \left(\frac{\frac{1}{2} - \nu}{1 + \nu} \right)^{1/2} \tag{12}$$

It is important to note that the reference paper uses a plastic Poisson's ratio here, but, since this parameter is not available for the foam in question, the Poisson's ratio from subsubsection 2.3.1 is used. With that in mind, the effective stress can be evaluated as:

$$\hat{\sigma}^2 = \frac{1}{1 + (\alpha/3)^2} \left[\sigma_v^2 + \alpha^2 \sigma_m^2 \right]. \tag{13}$$

2.4.3. Linear buckling

Linear buckling can be computed in `pyfe3d` as a generalised eigenvalue problem between the stiffness matrix $\mathbf{K_{C0_{uu}}}$, and the geometric stiffness matrix $\mathbf{K_{G_{uu}}}$, where the subscript $_{\mathbf{uu}}$, again, denotes application of boundary conditions [43]. The eigenvalue problem itself can be found for example in Castro et al. [44]:

$$(\mathbf{K_{C0_{uu}}} + \lambda \mathbf{K_{G_{uu}}})\mathbf{v} = \mathbf{0} \tag{14}$$

where $\mathbf{v}$ denotes an eigenvector and λ an eigenvalue. The smallest positive eigenvalue describes by what quantity the loads the structure is facing have to be multiplied to arrive at the critical buckling load. As per requirements (subsubsection 2.1.3), the load multiplier must be at least 1.5 for the considered design. The eigenvalue problem can be solved using `scipy.sparse.eigsh` [36, 45], since all matrices involved are symmetric.

2.4.4. Aeroelastic analysis

Following the method described in subsubsection 2.3.5, one can compute the aerodynamic matrix as the derivative of external aerodynamic forces with respect to displacements. It can be done by considering the structural displacements affecting the translations and rotations of the airfoils at the stations across the span in the VLM model, which, in turn, change the definition of the wing for the vortex lattice analysis.

$$\mathbf{K_A} = \frac{\partial \mathbf{F}}{\partial \mathbf{u}} = \frac{\partial \mathbf{F}}{\partial \mathbf{F_{VLM}}} \frac{\partial \mathbf{F_{VLM}}}{\partial \mathbf{p}} \frac{\partial \mathbf{p}}{\partial \mathbf{u}} \tag{15}$$

where $\mathbf{u}$ is the finite element displacement vector, $\mathbf{p}$ is the vector of flapwise translations of leading and trailing edges of airfoils at stations along the wing, and $\mathbf{F_{VLM}}$ is the vector of forces obtained from the vortex lattice method. The first term $\frac{\partial \mathbf{F}}{\partial \mathbf{F_{VLM}}}$ is an interpolation weight matrix, which can be obtained as described in subsubsection 2.3.5. The middle term $\frac{\partial \mathbf{F_{VLM}}}{\partial \mathbf{p}}$ can be obtained using a finite difference scheme, i.e. varying one value in $\mathbf{p}$ at a time and approximating a partial derivative. The final term $\frac{\partial \mathbf{p}}{\partial \mathbf{u}}$ is an interpolation matrix from displacements of the structural model to displacements of airfoil stations in the aerodynamic model. Instead of using a radial basis method, a single point of the structural mesh is assigned as a sample point for leading or trailing edge displacement of each airfoil station, with an interpolation weight of 2. The rationale behind this is presented in Appendix B.

With this aerodynamic matrix, one can apply boundary conditions, and, based on Guimarães et al. [14], write the equation of motion for an aeroelastic problem without damping:

$$(\mathbf{K_{C0_{uu}}} - \mathbf{K_{A_{uu}}} - \lambda \mathbf{M_{uu}})\mathbf{v} = \mathbf{0} \tag{16}$$

The aerodynamic matrix appears with a negative sign due to the way it is calculated: as a derivative of forces with respect to displacements, it would appear on the side of forces, so moving it to the left-hand side changes the sign. λ and $\mathbf{v}$ are again, an eigenvalue and an eigenvector. The onset of flutter or divergence is defined as when any natural frequency (square root of λ) attains a non-real value. Due to the aerodynamic matrix being asymmetric, one has to use a compatible solver such as the `scipy.sparse.eigs` [36, 45] to obtain the eigenvalues.

Naturally, one cannot obtain all eigenvalues of the large sparse system, so a region of interest (shift-invert value for the numerical solver and the number of eigenvalues requested), must be determined. Flutter can be expected to manifest itself in low-frequency oscillations, so the lowest-magnitude eigenvalues are of interest. That being said, the number of eigenvalues to find still remains unknown and has to be found experimentally.

The accuracy of the flutter prediction method is verified as described in Appendix C by comparison with the Goland wing benchmark [46]. Comparisons with both 2D induced airflow solutions [47, 48], unsteady VLM [49], and the original analytical solution reveal that the method presented in this study is in close agreement with other 2D methods.

2.4.5. Convergence Study

To determine the sufficient mesh resolution to obtain meaningful post-processing results, the simulation is conducted and post-processed for multiple values of N. Then, a mesh resolution from which further changes are considered negligible is selected for other simulations.

For stresses, the convergence criteria are ratios of equivalent to failure stresses for beam and quadrangular elements separately. This divide is due to different stress recovery techniques used for the two kinds of elements, and different equivalent stress calculations for the panel core. The stress convergence study is conducted for different values of the excluded area radius to chord ratio. The smallest value for which the stress ratios are convergent is selected for further simulations.

For buckling, it is vital to inspect the convergence of the load multiplier as well as the qualitative agreement between the buckling modes at different mesh resolutions. The mesh resolution is constrained both by the numerical proximity of the load multiplier to values at higher resolutions, but also by being constrained by the same modes as them. This additional criterion is necessary because a mesh resolution constrains the half-wavelength of the buckling modes that can be captured by the model [50].

Stress and buckling are evaluated for multiple load cases in this study. Theoretically, convergence could be checked for each of them at the expense of computational time. Instead, in this work, a test load case is conducted consisting of **LC3** with the addition of thrust from **LC0**. This allows for all investigated loads to be present in one load case. The challenge with this approach is that, while stresses can be superimposed in linear analysis [41, p.158], the linear buckling method is linear with respect to load only for uniform scaling. There are scenarios where the presence of additional loads changes the buckling behaviour profoundly, such as that of a pressurised cylinder [51]. The single load case approach has been selected because such a strong interaction between the thrust and the landing loads is not expected (the wingbox, being a beam, sees thrust mainly as shear and only locally as tension). Another reason is that during the optimisation process, the values of design variables change disproportionately, creating a qualitatively different model with potentially different buckling behaviour. It is thus impossible to formally evaluate the buckling convergence across the entire simulation domain, regardless of the number of load cases considered. In such a situation, the minimum test case deemed representative, a combination of **LC0** and **LC3**, is selected.

For the aeroelastic analysis, convergence of the natural frequencies is examined, as well as qualitative similarity between the vibration modes at different resolutions. The aeroelastic analysis is conducted for **LC2**, as during the main simulation. The convergence of the modes can be further examined using the Modal Assurance Criterion (MAC), which calculates the degree of similarity between two eigenvectors $\mathbf{v}_1$ and $\mathbf{v}_2$ [52]:

$$\mathrm{MAC} = \frac{(\mathbf{v}_1^\top \mathbf{v}_2)^2}{\mathbf{v}_1^\top \mathbf{v}_1 \mathbf{v}_2^\top \mathbf{v}_2} \tag{17}$$

A MAC value close to 0 indicates orthogonal modes, while a value close to 1 indicates that the two modes are scaled versions of each other [52]. For each value of N, the MAC between different modes can be computed. This allows for examining how the similarity between the modes changes with mesh refinement, providing a quantitative measure of the convergence of the vibration modes.

2.5. Iterative design and optimisation

The combination of finite element and aerodynamic simulation allows for examining the failure for a particular value of the design parameterisation. A numerical optimisation scheme is proposed to find a converged requirement-satisfying design. To that end, maximum stress, buckling load multiplier and natural frequency coalescence criteria are employed. In this study, the `COBYLA` [53] optimiser available in `scipy.minimize` [36] is employed. The algorithm is chosen because it is gradient-free. Thus, handling non-differentiable constraints such as maximum stresses across groups of elements should not hinder the convergence of this algorithm.

The vector of free variables used with their bounds corresponds to that of Equation 1. Before being passed to the optimiser, the design variables are normalised to values between zero and one, corresponding to their upper and lower bounds. This is to ensure the optimiser step size, which can only have a single value, remains relevant for every variable. The normalisation and de-normalisation are verified by de-normalising and normalising the design variable vector and comparing it with itself.

For each optimisation pass, an objective function is evaluated as the weight of the system computed from the mass matrix. Then, the constraint function is evaluated for failure modes and load cases identified as constraining prior to the optimisation. When the optimiser converges, the design is verified against all failure modes for each load case. The optimiser uses the mesh resolution found by the convergence study (subsubsection 2.4.5).

2.5.1. Sensitivity study

The critical assumptions made during the design concern the sandwich core and battery rail components. The rails are represented as booms with an effective diameter d (subsection 2.2), and the sandwich core as an isotropic material with a single failure stress criterion and a preliminarily estimated density ratio $\frac{\rho_{foam}}{\rho_{al}}$ (Equation 3). This is allowed under the justification that the focus of the work is on the global feasibility of the entire wing subsystem, and not on the design of its components. A sensitivity study is performed to ensure that those assumptions do not drive the result to an unacceptable extent and to explore the design space for the components.

While d can be directly varied as a single independent variable describing the rails, evaluating different foam cores is more involved. To obtain physically plausible materials, the altered variable is ρ_{foam}, and the foam stiffness and strength are re-computed from the Gibson-Ashby model for every density value. For each value of the assumed quantity, the optimisation process is re-conducted and the value of the objective function, i.e. the wingbox mass, is reported.

3. Results

First, a set of hyperparameters satisfying the battery volume constraints was found and reported in subsection 3.1 Then, convergence studies were conducted as reported in subsection 3.2. With a mesh resolution of $N = 12$ selected based on them, the sensitivity study was performed, yielding a sized design for different values of assumed parameters. This is described in subsection 3.4. All simulations were performed using Intel Core i7-1400F 5.4 GHz 28 MB Processor, ASUS Dual GeForce RTX 4060 Ti 8GB GPU and 6000 MHz 32 GB RAM. For readability reasons, only the most relevant of all generated results are directly included as figures. The complete implementation and simulation inputs and outputs are available in Gryszka and Castro [54].

3.1. Battery packing results

Due to the angled spar pattern fitting significantly better inside NACA 2418 than NACA 2419, the root thickness to chord has been reduced by 1% from the E9X baseline value. The final set of hyperparameters is shown in Table 3. For that set of hyperparameters, the half-wing could fit roughly 588 kg more of batteries than the required mass, indicating a roughly 3% margin for almost 17.5 tons of batteries per half-wing. The total thickness of the skin panels varies between 4.5 cm at the wing root and 1.8 cm at the wing tip, which is judged sufficient for leading pipes and wires through them.

The final battery layout is presented in Figure 5. There are 63 batteries inside each wing, indicating 22 min 51 s per battery during the 24-hour battery replacement imposed by **RB6**. Also, all batteries except one from the two most outboard rows are smaller than necessary to provide the 1 kV voltage necessary for **RB7**. As such, they would have to be connected in series to meet the requirement without introducing DC-DC conversion.

The most outboard row of the batteries is attached to the second and the third most outboard ribs, because the wing thickness further outboard was insufficient to satisfy the necessary clearances.

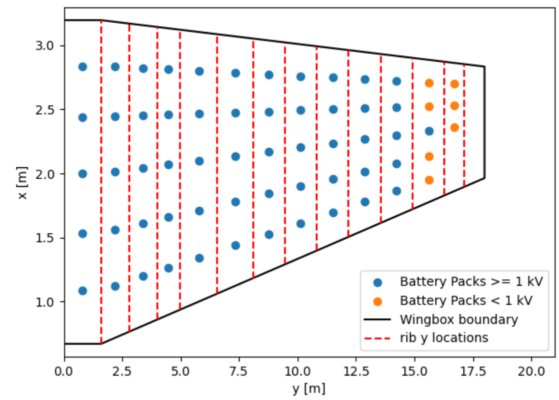

Figure 5: Positions of battery pack centroids inside the wingbox, indicating which packs can provide the required 1 kV voltage.

Table 3
Simulation settings for optimisation.

Quantity	Value	Unit
skin thickness ratio $(H/c)_{sq}$	0.009	-
spar thickness ratio $(H/c)_{pq}$	0.006	-
angled spar thickness ratio $(H/c)_{aq}$	0.003	-
battery rail diameter, d	0.03	m
battery chordwise clearance, δ	0.005	m
battery spanwise clearance, Δb	0.1	m
space for rail mount, D	0.3	m
nodes per sheet width, N	12	-
buckling eigenvalues examined	4	-
natural frequencies examined	30	-
airfoil stations	10	-
vortices spanwise between stations	20	-
vortices chordwise	10	-
interpolation coefficient, n_{points}	10	-
equipment mounting spring stiffness	10^{12}	N/m
out-of-plane hourglass control	1.7	-

Table 4
Values of the design variables used for the convergence studies.

Parameter	Value	Unit	Parameter	Value	Unit
$(2t/H)_{Sq}$	0.30	-	$(2t/H)_{sq}$	0.06	-
$(2t/H)_{Pq}$	0.25	-	$(2t/H)_{pq}$	0.3	-
$(2t/H)_{Aq}$	0.10	-	$(2t/H)_{aq}$	0.03	-
d_s	0.02	m	d_e	0.01	m
W_{bb}	0.01	m	W_{mb}	0.01	m
W_{lb}	0.02	m	-	-	-

3.2. Convergence studies

The convergence study is performed on values of the design variables from Table 4 and on the hyperparameter and simulation settings as given in Table 3, with the exception of the changed resolution parameter N.

The aeroelastic analysis was performed for ranges of N and `aerosandbox` model settings as described in Table 5, and

Table 5
Range of aeroelastic model parameters considered for convergence study.

Parameter	Minimum	Maximum
nodes per sheet width, N	5	12
airfoil stations	7	12
vortices spanwise between stations	15	20
vortices chordwise	7	10

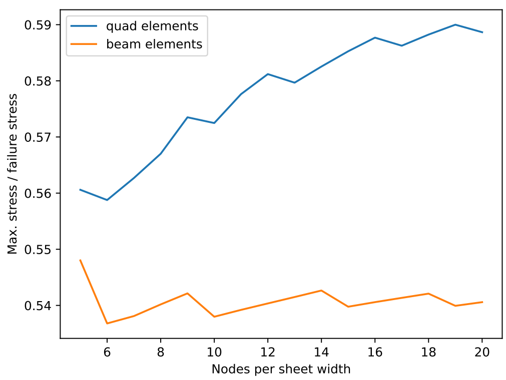

Figure 6: Convergence of the equivalent stress to failure stress margin.

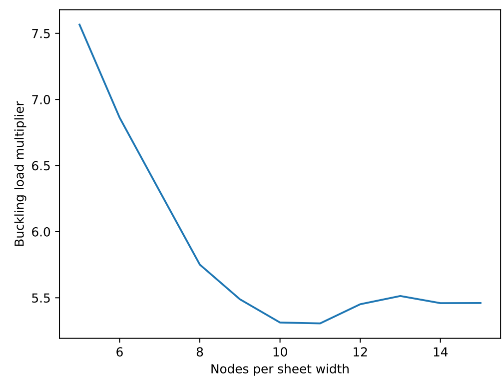

Figure 7: Convergence of the linear buckling load multiplier.

for n_{points} set to $\mathrm{floor}(N^2/4)$. This is to provide the required quadratic scaling but prevent large values of n_{points} for higher mesh resolution, which would have increased computational time. The first five natural frequencies obtained for different combinations of the varied parameters were of similar magnitude, and their coalescence was never observed. Visual inspection of the vibration modes for different N revealed no notable differences either. In light of that, MAC were computed between the first five modes for the examined range of N and presented in Table 6. The quantities reported in the table also do not experience significant changes over the examined range of N, confirming model stability for the aeroelastic analysis.

To establish the number of natural frequencies that needed to be recovered, the first thirty frequencies and modes were examined. The highest-frequency modes already showed local vibrations of the batteries and natural frequencies of several hundred rad/s, indicating the modes potentially involved in global flutter or divergence of the wing structure had already been taken into account within that number of recovered eigenvalues.

The stress and buckling analyses were conducted for the load case mentioned in subsubsection 2.4.5. The stress analysis was conducted up to $N = 20$ and was convergent starting from an excluded radius around joints of 0.0295 times the local chord length. The buckling analysis was conducted up to $N = 15$. While the overall change in the values of stress margin was smaller than that in load multiplier, the quad stress margin took longer to stabilise, hence, evaluating the larger N was necessary. The results are shown in Figure 6 and Figure 7. Based on the graphs, $N = 12$ was selected for further simulations, balancing proximity to results from more refined meshes and computational time. The first four buckling modes for $N = 12$ qualitatively correspond to those from $N = 15$.

To avoid hourglassing in buckling modes, the out-of-plane hourglass control factor for `Quad4R` is set to 1.7. The mounting spring stiffness is taken as a logarithmic-scale middle of the feasible interval between springs interfering with global vibrational modes and the model becoming ill-conditioned.

3.3. Optimised design

Based on evaluating all load cases on the same wingbox as used in subsection 3.2, the maximum stresses for **LC0** were considered critical and were the only constraints evaluated inside the optimisation loop. The optimisation concluded with success, returning a wingbox design variable vector as given in Table 7. The wingbox does not exhibit buckling, flutter or divergence, nor excess stress in any of the load cases. This verifies the choice of driving load cases for the optimisation.

The pull-up stresses for the optimised design are presented in Figure 8. The first four vibration modes of the wing are presented in Figure 9, while the driving buckling mode for **LC0**, with a load multiplier of 4.53, is shown in Figure 10.

3.4. Sensitivity study

The range of the sensitivity study is described in Table 8, at optimiser settings the same as for subsection 3.3, except for d in case of rail diameter sensitivity checks. The results of the sensitivity study are presented in Figure 11 and Figure 12. For $d = 0.1$, stresses from **LC3** became constraining as well.

4. Discussion

The primary goal in this section is to decide on the feasibility of the obtained design solution. To that end, the simulation results are interpreted in subsection 4.1 to assess

Table 6
Values of natural frequencies ω_n in rad/s and the Modal Assurance Criteria (MAC) between the first five modes of the aeroelastic system for N between 5 and 12.

N	5	6	7	8	9	10	11	12
$\omega_{n,\ 0}$	5.80	5.82	5.72	5.88	5.90	5.91	6.06	6.00
$\omega_{n,\ 1}$	18.92	18.92	18.93	18.93	18.93	18.93	18.93	18.93
$\omega_{n,\ 2}$	23.40	23.30	23.35	23.34	23.34	23.35	23.43	23.42
$\omega_{n,\ 3}$	36.75	36.68	36.68	36.66	36.66	36.65	36.69	36.68
$\omega_{n,\ 4}$	52.47	52.41	52.38	52.36	52.34	52.34	52.33	52.32
$\mathrm{MAC}_{0,\ 1}$	0.026	0.027	0.027	0.027	0.027	0.028	0.028	0.028
$\mathrm{MAC}_{0,\ 2}$	0.073	0.075	0.075	0.073	0.074	0.076	0.078	0.079
$\mathrm{MAC}_{0,\ 3}$	0.304	0.305	0.306	0.306	0.308	0.309	0.312	0.313
$\mathrm{MAC}_{0,\ 4}$	0.032	0.032	0.034	0.035	0.035	0.037	0.039	0.038
$\mathrm{MAC}_{1,\ 2}$	0.000	0.000	0.000	0.000	0.000	0.000	0.000	0.000
$\mathrm{MAC}_{1,\ 3}$	0.001	0.001	0.001	0.001	0.001	0.001	0.001	0.001
$\mathrm{MAC}_{1,\ 4}$	0.007	0.007	0.007	0.007	0.007	0.008	0.008	0.008
$\mathrm{MAC}_{2,\ 3}$	0.001	0.001	0.001	0.000	0.000	0.001	0.001	0.001
$\mathrm{MAC}_{2,\ 4}$	0.000	0.000	0.000	0.000	0.000	0.000	0.000	0.000
$\mathrm{MAC}_{3,\ 4}$	0.066	0.066	0.070	0.074	0.074	0.075	0.081	0.080

Table 7
Values of the design variables of the optimised wingbox.

Parameter	**Value**	**Unit**	**Parameter**	**Value**	**Unit**
$(2t/H)_{Sq}$	0.158	-	$(2t/H)_{sq}$	0.157	-
$(2t/H)_{Pq}$	0.154	-	$(2t/H)_{pq}$	0.112	-
$(2t/H)_{Aq}$	0.147	-	$(2t/H)_{aq}$	0.111	-
d_s	0.012	m	d_e	0.012	m
W_{bb}	0.016	m	W_{mb}	0.016	m
W_{lb}	0.016	m	-	-	-

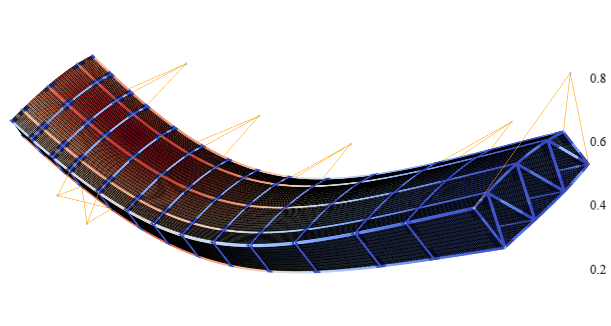

Figure 8: Map of maximum stress to failure stress ratio across the optimised wing for **LC0**.

Table 8
Inputs to the sensitivity study.

Variable	**Unit**	**Baseline**	**Min.**	**Max.**	**Samples**
ρ_{foam}	kg/m^3	250.2	100.0	400.0	5
d	m	0.03	0.01	0.05	5

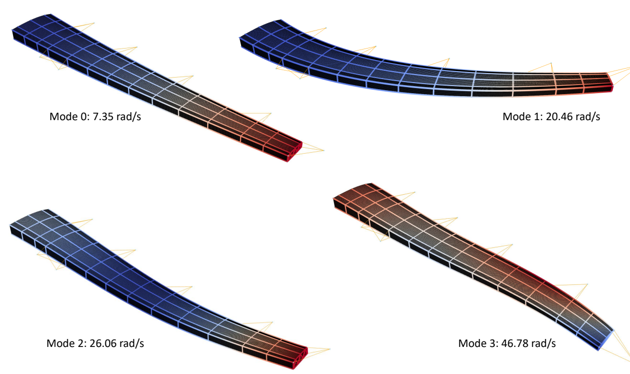

Figure 9: Overview of the first four vibrational modes and natural frequencies of the optimised wingbox. These modes are first flapwise bending, first chordwise bending, second flapwise bending and first torsion, respectively.

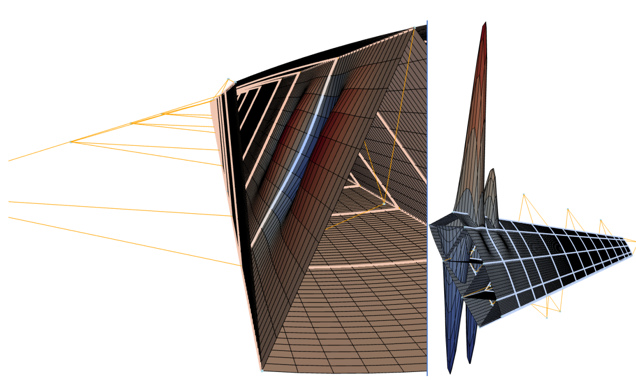

Figure 10: First buckling mode for **LC0**. The mode involves buckling of the most fore-angled spar across the second inboard truss rib.

their plausibility as well as explain the behaviour of the structure. Then, limitations of the analyses used are outlined in subsection 4.2. In light of that, the results of this study are compared against previous analyses of the E9X wing in subsection 4.3. In subsection 4.4, a compliance matrix for the battery integration requirements is constructed. With all of the above considered, a final verdict on design feasibility

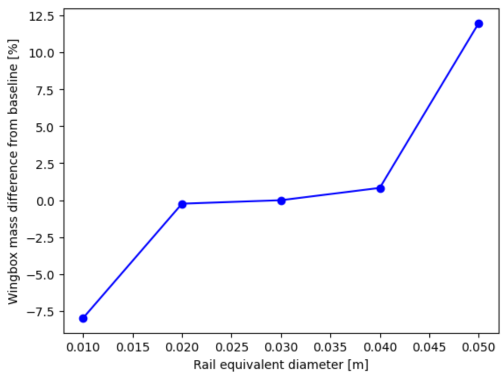

Figure 11: Sensitivity of wingbox mass to changing the equivalent rail diameter d.

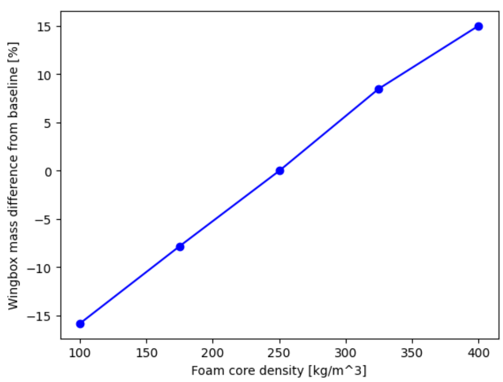

Figure 12: Sensitivity of wingbox mass to changing the foam core density ρ_{foam}.

is reached in subsection 4.5 and the second iteration of the design is proposed in subsection 4.6.

4.1. Simulation result analysis

The stress distributions, vibration and buckling modes obtained in subsection 3.3 provide qualitative insights into the structural behaviour, while sensitivity study results from subsection 3.4 can be interpreted to indicate targets for subsystem design.

4.1.1. Structural performance of the wingbox

From the design variable vector in Table 7, it can be seen that all provided reinforcement options (ribs, spanwise reinforcements, skin thickness ratios) are used by the optimiser, with no variables close to their lower or upper bounds. The landing load case is non-driving, contrary to expectations.

It is notable that the elastic failure modes, such as buckling and aeroelastic flutter/divergence, are significantly less constraining than maximum stress limits. This is attributed to the use of sandwich panels increasing the local out-of-plane stiffness of the wingbox sheets. The truss-ribs themselves, as expected, are less effective in reducing the wingbox effective length than their sheet metal counterparts. In Figure 10, the buckling mode occurs across the ribs.

As for the aeroelastic failure modes, their absence is attributed to torsional modes being hard to excite for the multi-cell wingbox. As seen in Figure 9, the first torsional mode of the wing is fourth overall, with chordwise bending and the second flapwise bending mode having lower natural frequencies.

Overall, the results point to excessive stiffness of the current design iteration. Future design iterations should thus focus on removing the excess stiffness together with its associated excess mass. This can be accomplished by altering the design of the angled spars. Possible suggestions are sizing the angled spars independently (the most constraining buckling mode occurred on the most fore-angled spar, so others can be thinned), or switching to stiffened webs for (some of) the spars, while remaining with sandwich panels for the skins. Such design changes may require a larger range of thicknesses or manufacturing techniques to be employed, creating a trade-off between weight and complexity.

4.1.2. Implications of sensitivity study results on subsystem design

As can be seen from Figure 11, the overall wingbox mass is plateaued for values of d between 20 and 40 mm. Within this range, d can be selected primarily based on rail requirements, without significantly impacting the overall structural mass. Even lower d would be significantly beneficial, although it cannot be guaranteed due to rails needing to withstand the battery load.

As for the core density (Figure 12), its effect is larger than that of d and monotonous. The mass clearly continues to decrease when lowering core density past the initial guess of matching yield stresses. In the Gibson-Ashby model, the foam stiffness decreases with density faster than its strength. As such, a lighter sandwich core is farther from its failure point than a heavier one under the same load, while a larger portion of the load is carried by the skin. Considering that the core of the provided design contains numerous cutouts and channels, and thus a risk of local imperfections is high, having this larger margin to failure is of interest.

The behaviour of the core, however, changes significantly with its material and manufacturing method. Given its profound effect on the overall structural mass, it is necessary to select the core material for further design. Next to foam core with cutouts assumed in this study, a prospective option might be using a locally reinforced honeycomb (especially if next iterations of the design are expected to have fewer channels through the core, as suggested in subsection 4.6), or 3D printing the core [55] with its strength and interior varying locally.

4.2. Limitations

Due to their simplified nature, the methods employed in this study carry significant limitations. While justified for initial analysis, those deficiencies need to be addressed in future work on the design. Overall, the following method limitations have been identified:

- **Exclusively linear analysis**. A linear structural model cannot capture nonlinear effects. This includes the Brazier effect [4, p.596], which entails ovalisation of the cross-section under bending. Including such nonlinear effects would be necessary to fully assess the shape-preservation performance of the angled spars. Another feature of linear models is constant stiffness and aerodynamic matrices, which prevents modelling different tensile and compressive responses of the panel core, the exact reaction forces at equipment supports, and non-linearity in lift generation by the deforming wing;

- **Exclusively static undamped analysis**, which affects the aeroelastic and landing load predictions;
- **Simplified modelling of the sandwich panel failure**. Next to the considered skin and core failure, there is also the possibility of adhesion failure, wrinkling (local skin buckling), and other core-related failure modes [56];
- **Only global geometrical features included in the analysis**. This means skipping the effects of wire channels, heated insert rows, access holes and local sections made from a different material than the baseline aluminium. The effect of this simplification is clearly non-conservative, as many such features cause local stress concentrations and/or require interfaces that increase mass;
- **Not modelling the fuselage cutout for battery extraction**. This part of the aircraft needs to be heavily reinforced, significantly influencing the total mass.

There are also several shortcomings of the proposed design concept, outlining aspects in which it fails to meet its intended design objectives. These are, in order of decreasing importance:

- **Excess stiffness and weight created by the angled spars**, whose presence is mandated as reinforcement for the battery packs and for wing cross-section shape preservation;
- **Heavily limited ability to allow for built-in wing twist** for the rails to remain straight, and the battery volume being sufficient;
- **Wingbox width dictated by angled spars and close-packed batteries**. This is the reason the root thickness to chord has to be reduced by one percent point for this design (see subsection 3.1);
- **High number of battery packs compared to a standard wingbox.** This complicates battery replacement logistics, further discussed in subsection 4.4.

While it is clear that the proposed design concept cannot work with a built-in twist and constrains the internal layout of the wing structure, it is currently unclear whether there is a concept of battery placement in the wing that would allow for complete wing design freedom. Related studies, Kemperink [5] and de Vries et al. [7] establish that the presence of batteries severely constrains the wing design space, choosing for the battery-housing portion of the wing to remain straight and untapered. Contrastingly, the solution proposed in the present study offers design freedom in a different direction of aerodynamic design.

4.3. Comparison with existing literature

Since no absolute estimate of wing mass for the E9X is publicly available, a direct structural performance comparison between the proposed concepts is impossible. Instead, the findings of related studies are mentioned, and any discrepancies between their results and those of the present study are addressed.

4.3.1. The initial E9X design

The wingbox design presented herein, for the default d and core density value, results in a wing mass 8-13% higher than that of de Vries et al. [1]. While the results of this study agree that bending relief from the batteries is significant, and the landing and aeroelastic loads originally labelled as risks have proven manageable, the effect of modifications needed to make batteries replaceable remains comparably profound. This verdict might change upon further optimisation to reduce the excess stiffness noticed in subsubsection 4.1.1.

The mass difference is obtained as follows. As the angled spar wingbox features vertical edge spars, it is assumed that the part of the wing not housing batteries, such as the leading edge or the wing tip, can remain of conventional design. Thus, the difference in the wing masses is assumed to be the difference in wingbox masses. The wingbox mass of the original design is then recovered from the provided Class II results. This is done using Equations 107 and 109 from Ardema et al. [57], which provide statistical regressions between wingbox mass and wing mass, or wingbox mass and wing plus movable surface mass, respectively. 8% increase results from recovering the original wingbox mass from the wing structural mass only, while the 13% increase is obtained using the equation that also considers movable surfaces.

4.3.2. E9X wing design when not accounting for battery replacement

Wang et al. [8] conducted E9X wing structural design based on the first-iteration planform geometry. The presence of batteries in the wing is accounted for, but their operational requirements are not, and battery replacement is not mentioned. Thus, only *Challenge II* is treated in isolation from *Challenge I*.

The study reports significant bending relief coming from the presence of batteries, finds, similarly to the current study, that landing and aeroelastic load cases are fully addressable, and converges to a wide, two-spar wingbox. Comparing the optimal geometry found by the study with the angled spars solution, it can be conjectured that *Challenge II*, when considered separately from *Challenge I*, can lead to overly optimistic structural performance predictions.

Comparing driving load cases between this study and Wang et al. [8], there is agreement that aeroelastic flutter or divergence are less significant than stress or buckling. The wing tip of the *Challenge II* only design, however, is constrained by buckling, while for the angled spars, only stress is constraining. This would agree with the notion of excess stiffness being present in the angled spars design.

4.3.3. The openable rib concept

The current design offers significantly more aerodynamic design freedom than the openable rib design by Kemperink [5], allowing for significant taper, moderate wing sweep and dihedral while strictly limiting wing twist. Both designs allow for a variable thickness-to-chord ratio. The only constraint posed by the angled spars design, not posed by the openable rib one, is the constraint on the wingbox width (see subsection 4.2).

While no global wing design is performed by Kemperink [5], the wingbox with openable ribs is still a conventional one, hence its mass is expected to be one yielded by the estimates from Wang et al. [8], with a penalty resulting from the presence of rib hinges and dove-tail connections. Both battery removal concepts are affected by the presence of rails and battery extraction cutouts in a similar way. On that ground, the angled spars may be heavier than the design proposed by Kemperink [5], but that would have to be confirmed by completing the design of the openable-rib wingbox. The wide rectangular wingbox of the design proposed by Kemperink [5] houses a smaller number of larger battery packs, allowing for simpler and potentially faster replacement procedures.

As such, it can be stated that the design developed in this study allows for noticeably more freedom in wing aerodynamic design and elimination of openable ribs, while Kemperink [5] prioritises unconstrained spar locations, similarity to conventional wingbox, and rapid battery replacement.

Another observation is that it is the usage of monorail combined with side battery supports instead of duorail that increases the freedom of wing design by removing the parallel rails constraint, while the solution of the angled spars allows for avoiding movable wingbox sheets. Thus, the design choices between Kemperink [5] and this study could be recombined to achieve a compromise design between those two.

4.3.4. The second-iteration E9X design

The new wing design of the E9X presented by de Vries et al. [7] features a large rectangular section, which favours the openable rib solution proposed by Kemperink [5]. That being said, the simplified wing allows for a unified size of the battery packs, which would benefit the logistics of the angled spar as well. For a straight wing, subdividing the prismatic battery packs into modules might prove feasible, as is done for rectangular battery packs systems [3]. Nonetheless, the angled spars were planned for the initial E9X wing, and the concept would need substantial refinement to be adapted to the new wing geometry in a viable manner.

4.4. Compliance with the battery requirements

The compliance of the proposed design with the battery requirements is summarised in Table 9. When applicable, a metric associated with the requirement is defined and quantified. At this stage of the design, it is not possible to guarantee compliance with **RB6** and **RB7**. However, values of their metrics specify constraints within which the later design has to fit to satisfy them.

Table 9
Compliance with battery requirements. Requirements that are judged as satisfied are marked in blue.

ID	Metric	Value	Reference
RB1	Extra battery mass	588 kg	subsection 3.1
RB2	-	-	subsubsection 2.2.1
RB3	-	-	subsubsection 2.2.1
RB4	-	-	subsubsection 2.3.1
RB5	-	-	subsubsection 2.2.1
RB6	Time per pack	23 min	subsection 3.1
RB7	Packs in series	7	subsection 3.1
RB8	-	-	subsubsection 2.2.1

The replacement time per battery pack (understood as a single prism between two angled spars and two truss ribs) includes removing the old battery, inserting a new one and performing the necessary checks. This may lead to the almost 23 minutes being insufficient, which can be addressed by removing batteries from two different cells in parallel. Nonetheless, the complexity of the replacement procedure is significantly higher than for a single-cell wingbox, either due to time constraints or by having to coordinate parallel work in a constrained space.

Similarly, the need to connect the seven smallest battery packs in series, although not impossible, is expected to complicate the wiring around the wing tip when the sandwich panels are at their thinnest. Should that prove to be a concern, it can be addressed by using the free space available at the wing tip. The spanwise section closest to the wing tips had insufficient space to house the batteries, which left it unoccupied. The resultant space can be used to guide the wires through.

4.5. Final verdict on design feasibility

The design cannot be judged as feasible unconditionally, as so far only simplified methods have been used to size its first iteration. Nevertheless, several arguments for and against the feasibility of the concept can already be proposed.

The design is capable of meeting all of its requirements, both battery and structural. There is a large margin for buckling and aeroelastic failure modes, and none of the skin thicknesses has reached its maximum value during the optimisation. Therefore, there is a margin in case more detailed analyses yield more constraining results. The project objectives of no primary structure disassembly and preserving the aerodynamic design freedom of the wing are, to a large extent, satisfied, with the only free variable that had to be constrained being the wing twist. Furthermore, the concept can be further optimised, for example, by increasing the number of free variables and adapting less conservative spar thicknesses.

On the other hand, the design may be heavier than the Class II weight estimates presented by de Vries et al. [1], and its subsystems, such as the prismatic battery packs, battery rails and sandwich panel skins, are complex and unconventional. This offsets the gains from avoiding rib openings and preserving the trapezoidal wing. As such, the concept is judged to be technically feasible, but unlikely to achieve better performance or a smoother development path than the openable rib concept proposed by Kemperink [5].

4.6. Outline of the second iteration of the design

The main issue of the first iteration was its complexity. Second, there seems to be a weight penalty associated with the design. Both can be seen as driven primarily by the multi-cell nature of the wingbox, which is in turn driven by the usage of the close-packed hexagonal battery packs. This battery pack configuration was selected for efficient usage of the wingbox volume and regular design of the battery packs themselves. In light of the increased battery volume in the new E9X iteration [7], this design choice may be reconsidered.

Analysis of the first iteration revealed excessive wingbox stiffness, resulting from the sandwich panels used as stiffness compensation for the ribs performing better than expected, and the aircraft torsional response also being harder to excite than presumed. In the redesign, a less conservative set of hyperparameters can be adopted, and a lower number of spars should be aimed for.

An initial idea for the second iteration of the angled spars concept is outlined in Figure 13. In the new concept, there is a single angled spar separating two battery packs made from rectangular modules. Such a setup allows for simpler wiring and is significantly closer to a conventional wingbox. While the skins likely need to remain sandwich panels for buckling concerns, other structures can be explored for the spars.

The main risk envisioned for the second iteration is worse performance with respect to the Brazier effect, aeroelasticity and spar buckling, necessitating inclusion of relevant analyses in the optimisation loop and thus significantly increasing the computational time. Design of certain subsystems, such as thermal runaway ventilation, might prove difficult due to the irregular assembly of battery modules. It is thus possible that a middle-ground solution between the two iterations is adopted, but the details of the compromise between the two cannot be specified without further analysis.

5. Conclusion

This work aimed to find a wingbox design satisfying battery requirements, most importantly those posed by battery replacement, for a large all-electric aircraft. Specifically, the possibility of a design not requiring part of the primary structure to open during the replacement procedure was examined. The first iteration of Elysian Aircraft E9X was considered as a case study.

Next to structural constraints, such as aeroelastic and buckling stability and stress margins, battery requirements, such as their mass, necessary subsystem connections and

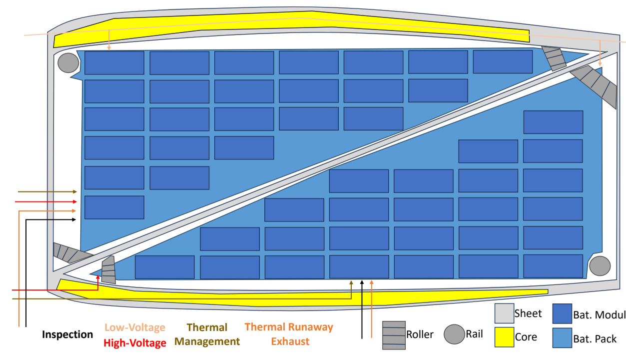

Figure 13: Outline of the proposed second iteration of the design.

replacement logistics were investigated. To satisfy them, an angled spar wingbox design was proposed that replaced ribs with trusses and reinforced the structure with additional angle spars. Prismatic battery packs were to be moved spanwise using monorail lead screw rails, allowing for extraction at the wing root. The skins and spars of the wingbox were to be made from sandwich panels, allowing to establish the necessary subsystem connections through their core. Instead of conducting subsystem design, equivalent rail diameter and sandwich core density were subject to sensitivity study. The design allowed for wing taper, thickness-to-chord, dihedral and sweep to be nonzero, accommodating a general untwisted trapezoid wing conditional on sufficient battery volume.

A preliminary model of such an angled-spar wingbox was analysed in `pyfe3d` and `aerosandbox`. For the purpose of the analysis, a linear flutter analysis was developed and verified with the Goland wing benchmark, and custom stress recovery for the sandwich panel and beam elements used was implemented. The analysis revealed that the current, partially optimised design is strength- not stiffness-constrained and that the wing is 8-13% heavier than the original E9X class II estimates. While capable of meeting its requirements, the viability of the design was considered questionable due to its complexity and weight. A subsequent redesign with goals of reducing weight together with the excess stiffness, simplification and adapting to the second-iteration E9X geometry was suggested.

Important limitations of this study involve using simplified core and rail modelling, as well as global, static and linear finite element and aerodynamic models. Further work will focus on addressing those by investigating the Brazier load, and conducting subsystem design that would allow for calibrating the global models.

Overall, although with a heavily constrained design space and related weight and complexity penalties, it is possible to design a large aircraft wingbox whose batteries can be replaced without opening large areas of its walls.

6. Acknowledgements

This work has been performed as part of the Honours Program Bachelor's at Delft University of Technology. The authors would like to thank Hidde Kemperink for his prior research and advice, Dr.ir. Reynard de Vries and Dr. ir. Roelof Vos for the E9X data, Teo Cokonaj for his feedback on the paper and Piotr Gryszka for providing the main harware used for the simulations, and for helping with running the simulations.

References

[1] Reynard de Vries, Rob E. Wolleswinkel, Maurice Hoogreef, and Roelof Vos. A new perspective on battery-electric aviation, part ii: Conceptual design of a 90-seater. In *AIAA SCITECH Forum*, 2024. doi: https://doi.org/10.2514/6.2024-1490.

[2] Rob E. Wolleswinkel, Reynard de Vries, Maurice Hoogreef, and Roelof Vos. A new perspective on battery-electric aviation, part i: Reassessment of achievable range. In *AIAA SCITECH Forum*, 2024. doi: https://doi.org/10.2514/6.2024-1489.

[3] Electric Power systems. *EPiC Energy Propulsion Battery System. Product Specifications*, 2023.

[4] C. R. Calladine. *The Brazier effect in the buckling of bent tubes*, page 595–625. Cambridge University Press, 1983.

[5] H. H. A. Kemperink. Rapid exchange of battery packs in aircraft wings. Master's thesis, Delft University of Technology, Faculty of Aerospace Engineering, 2025. URL https://resolver.tudelft.nl/uuid:e6588271-9931-4719-b82b-ed9ff90a8e61.

[6] Higor Luis Silva, Thiago A. Guimarães, and Saullo G. P. Castro. Design and aeroelastic analysis of truss-based modular wing structures. In *AIAA SCITECH Forum*, 2023. URL https://arc.aiaa.org/doi/10.2514/6.2023-1677.

[7] Reynard de Vries, Rob E. Wolleswinkel, Joaquin Exalto, Pieter van den Berg, Roelof Vos, and Maurice Hoogreef. Conceptual redesign of a 90-seater battery-electric aircraft. In *AIAA AVIATION Forum and ASCEND*, 2025. doi: https://doi.org/10.2514/6.2025-3153.

[8] Z. Wang, R. De Breuker, and J. Sodja. A study on wing structural design and sizing for a large battery-electric aircraft. In *AIAA SCITECH Forum*, 2025. doi: https://doi.org/10.2514/6.2025-3470.

[9] European Union Aviation Safety Agency. Third publication of means of compliance with the special condition vtol, moc-3 sc-vtol. Technical Report Issue 2, European Union Aviation Safety Agency, Cologne, Germany, June 2023.

[10] Janine Ebersberger, Leon Fauth, Ralf Keuter, Yongtao Cao, Yannik Freund, Richard Hanke-Rauschenbach, Bernd Ponick, Axel Mertens, and Jens Friebe. Power distribution and propulsion system for an all-electric short-range commuter aircraft - a case study. *IEEE Access*, 2022. doi: https://doi.org/10.1109/ACCESS.2022.3217650.

[11] Richard D. Alexander, Danielle Meyer, and Jiankang Wang. A comparison of electric vehicle power systems to predict architectures, voltage levels, power requirements, and load characteristics of the future all-electric aircraft. In *2018 IEEE Transportation Electrification Conference and Expo (ITEC)*, pages 194–200, Long Beach, CA, USA, 2018. IEEE. doi: https://doi.org/10.1109/ITEC.2018.8450240.

[12] Amir H. Naghshineh-Pour. Structural optimization and design of a strut-braced wing aircraft. Master's thesis, Virginia Polytechnic Institute and State University, 1998. URL https://vtechworks.lib.vt.edu/items/ee273cd0-c75e-43b1-9693-4388693e7d07.

[13] European Union Aviation Safety Agency. Certification specifications and acceptable means of compliance for large aeroplanes (cs-25), amendment 27. Technical report, European Union Aviation Safety Agency, 2022. URL https://www.easa.europa.eu/en/document-library/easy-access-rules/easy-access-rules-large-aeroplanes-cs-25.

[14] Thiago A. M. Guimarães, Saullo G. P. Castro, Domingos A. Rade, and Carlos E. S. Cesnik. Panel flutter analysis and optimization of composite tow steered plates. In *58th AIAA/ASCE/AHS/ASC Structures, Structural Dynamics, and Materials Conference*, 2017. doi: https://doi.org/10.2514/6.2017-1118.

[15] T. H. G. Megson. *Aircraft Structures for Engineering Students*. Butterworth-Heinemann, Oxford, UK, 4 edition, 2007. ISBN 978-0-7506-6739-5.

[16] Gabriel LaPlante, Andrew E. Marble, Bryce MacMillan, Pearl Lee-Sullivan, Bruce G. Colpitts, and Bruce J. Balcom. Detection of water ingress in composite sandwich structures: a magnetic resonance approach. *NDT & E International*, 2005. URL https://www.sciencedirect.com/science/article/abs/pii/S0963869505000216.

[17] Hiromu Okamoto, Masayoshi Suhara, Ryuichi Nagase, Toshikazu Shigetomi, and Morimasa Ishida. Aircraft reinforcing structure, March 2021. URL https://patents.google.com/patent/US10940937B2/en.

[18] D. M. Jensen and L. H. Hihara. The effect of corrosion on the delamination of carbon-fiber/epoxy and e-glass-fiber/epoxy polymer-matrix composites on various aluminum alloy substrates due to exposure of the gm-9540p accelerated corrosion test. Technical Report Paper No. 2017-984532, Defense Acquisition University (DAU), 2017. URL https://www.dau.edu/sites/default/files/Migrated/CopDocuments/The%20Effect%20of%20Corrosion%20on%20the%20Delamination%20of%20Carbon-Fiber%20and%20Epoxy%20and%20E-Glass-Fiber%20and%20Epoxy%20Polymer-Matrix%20Composites.pdf.

[19] Ltd. Energy Business Division Samsung SDI Co. Specification of product. lithium-ion rechargeable cell for power tools. model name: Inr21700-40t, 2017. URL https://www.dnkpower.com/wp-content/uploads/2019/02/SAMSUNG-INR21700-40T-Datasheet.pdf.

[20] Saullo G. P. Castro. General-purpose finite element solver based on Python and Cython, 2026. URL https://doi.org/10.5281/zenodo.6573489.

[21] Peter D. Sharpe. Aerosandbox: A differentiable framework for aircraft design optimization. Master's thesis, Massachusetts Institute of Technology, 2021. Available at https://dspace.mit.edu/handle/1721.1/140023.

[22] Peter D. Sharpe. *Accelerating Practical Engineering Design Optimization with Computational Graph Transformations*. PhD thesis, Massachusetts Institute of Technology, 2024. Available at https://dspace.mit.edu/handle/1721.1/157809.

[23] S.P. Timoshenko. X. on the transverse vibrations of bars of uniform cross-section. *The London, Edinburgh, and Dublin Philosophical Magazine and Journal of Science*, 43(253):125–131, 1922. doi: https://doi.org/10.1080/14786442208633855.

[24] Norbert Geier. An experimental study on the drilling of cfrp sandwich structures with filled and unfilled aramid honeycomb cores. *Journal of the Brazilian Society of Mechanical Sciences and Engineering*, 45 (4):219, 2023. doi: https://doi.org/10.1007/s40430-023-04138-5.

[25] E. Andrews, W. Sanders, and L.J. Gibson. Compressive and tensile behaviour of aluminum foams. *Materials Science and Engineering: A*, 270(2):113–124, 1999. URL https://www.sciencedirect.com/science/article/abs/pii/S0921509399001707.

[26] L. J. Gibson and M. F. Ashby. *Cellular Solids: Structure and Properties*. Cambridge University Press, Cambridge, UK, 2 edition, 1997. ISBN 9780521499118.

[27] ASM. Aluminum 2024-t81, 2024. URL https://asm.matweb.com/search/SpecificMaterial.asp?bassnum=MA2024T81. Accessed: 2025-12-1.

[28] Jaroslav Kováčik, Liviu Marsavina, and Emanoil Linul. Poisson's ratio of closed-cell aluminium foams. *Materials*, 2018. doi: https://doi.org/10.3390/ma11101904.

[29] Adrian Haas. PyPardiso: Python interface to the Intel MKL Pardiso library. https://github.com/haasad/PyPardiso, 2025. Version 0.4.7.

[30] Krzysztof Śledziewski. Fatigue assessment for selected connections of structural steel bridge components using the finite elements method. *AIP Conference Proceedings*, 1922(1):150001, 01 2018. ISSN 0094-243X. doi: https://doi.org/10.1063/1.5019154.

[31] U.S. Department of Defense. Bolts, aircraft. Military Specification MIL-B-6812E, U.S. Department of Defense, April 1994.

[32] Lingyu Zhou, Liping Wang, and Liqiang Jiang. Chapter 4 - bolted joints in steel structures. In *Design of Steel Structures*, pages 133–173. Elsevier, 2022. ISBN 978-0-323-91682-0. doi: https://doi.org/10.1016/B978-0-323-91682-0.00018-2. URL https://www.sciencedirect.com/science/article/pii/B9780323916820000182.

[33] Great Steel and Metals. Astm a193 grade b7 bolts, 2024. URL https://www.greatmetal.com/astm-a193-grade-b7-bolts-fasteners.html. Accessed: 2026-05-31.

[34] Witten Company. Nas1833 insert, molded in, threaded, self-locking/nonself-locking, sandwich panel. Technical Datasheet, October 2022. Revision B, Approval Date: 2022-10-19, GAGE Code 0JHK5.

[35] John D. Anderson. *Fundamentals of Aerodynamics*. McGraw-Hill, New York, 5 edition, 2010. ISBN 9780073398105.

[36] Pauli Virtanen, Ralf Gommers, Travis E. Oliphant, Matt Haberland, Tyler Reddy, David Cournapeau, Evgeni Burovski, Pearu Peterson, Warren Weckesser, Jonathan Bright, Stéfan J. van der Walt, Matthew Brett, Joshua Wilson, K. Jarrod Millman, Nikolay Mayorov, Andrew R. J. Nelson, Eric Jones, Robert Kern, Eric Larson, C J Carey, İlhan Polat, Yu Feng, Eric W. Moore, Jake VanderPlas, Denis Laxalde, Josef Perktold, Robert Cimrman, Ian Henriksen, E. A. Quintero, Charles R. Harris, Anne M. Archibald, Antônio H. Ribeiro, Fabian Pedregosa, Paul van Mulbregt, and SciPy 1.0 Contributors. SciPy 1.0: Fundamental Algorithms for Scientific Computing in Python. *Nature Methods*, 2020. doi: https://doi.org/10.1038/s41592-019-0686-2.

[37] Songrit Maneewongvatana and David M Mount. Analysis of approximate nearest neighbor searching with clustered point sets. In *Data Structures, Near Neighbor Searches, and Methodology: Fifth and Sixth DIMACS Implementation Challenge*, pages 105–123. American Mathematical Society, 1999.

[38] Yunhua Luo. An efficient 3d timoshenko beam element with consistent shape functions. *Advances in Theoretical and Applied Mechanics*, 1(3):95–106, 2008. URL https://www.m-hikari.com/atam/atam2008/atam1-4-2008/luoATAM1-4-2008-1.pdf.

[39] Engineering at Alberta Courses. Stress: Stress based failure criteria, n.d. URL https://engcourses-uofa.ca/books/introduction-to-solid-mechanics/stress/stress-based-failure-criteria/. Accessed: 2025-11-26.

[40] Terje Haukaas. Kirchhoff and mindlin plates, 2019. URL https://civil-terje.sites.olt.ubc.ca/files/2019/06/Kirchhoff-and-Mindlin-Plates.pdf. Accessed: 2025-11-26.

[41] Russer Charles Hibbler. *Mechanics of Materials. Tenth Edition in SI Units.* Pearson, 2018. ISBN 9781292178202.

[42] G Gioux, T.M McCormack, and L.J Gibson. Failure of aluminum foams under multiaxial loads. *International Journal of Mechanical Sciences*, 42(6):1097–1117, 2000. URL https://www.sciencedirect.com/science/article/abs/pii/S0020740399000430.

[43] Saullo G. P. Castro. pyfe3d — Linear buckling analysis of a cylinder under torsion, 2025. URL https://saullocastro.github.io/pyfe3d/ex_linear_buckling_cylinder_torsion.html. Accessed: 2025-11-26.

[44] Saullo G. P. Castro, Christian Mittelstedt, Francisco A.C. Monteiro, Mariano A. Arbelo, Gerhard Ziegmann, and Richard Degenhardt. Linear buckling predictions of unstiffened laminated composite cylinders and cones under various loading and boundary conditions using semi-analytical models. *Composite Structures*, 2014. doi: https://doi.org/10.1016/j.compstruct.2014.07.037.

[45] R. B. Lehoucq, D. C. Sorensen, and C. Yang. *ARPACK Users' Guide: Solution of Large Scale Eigenvalue Problems with Implicitly Restarted Arnoldi Methods*. SIAM, Philadelphia, PA, 1998. ISBN 9780898714074.

[46] Martin Goland. The flutter of a uniform cantilever wing. *Journal of Applied Mechanics*, 1945. doi: https://doi.org/10.1115/1.4009489.

[47] Zahra Sotoudeh, Dewey H. Hodges, and Chong-Seok Chang. Validation studies for nonlinear aeroelastic trim and stability analysis of highly flexible aircraft. *Journal of Aircraft*, 2010. doi: https://doi.org/10.2514/1.46974.

[48] Rafael Palacios and Bogdan I. Epureanu. An intrinsic description of the nonlinear aeroelasticity of very flexible wings. In *52nd AIAA/ASME/ASCE/AHS/ASC Structures, Structural Dynamics, and Materials Conference*, Denver, Colorado, USA, 2011. doi: https://doi.org/10.2514/6.2011-1917.

[49] Joseba Murua, Rafael Palacios, and J. Michael R. Graham. Modeling of nonlinear flexible aircraft dynamics including free-wake effects. In *AIAA Atmospheric Flight Mechanics Conference*, 2010. doi: https://doi.org/10.2514/6.2010-8226.

[50] Oluwole K Fajuyitan, Adam J Sadowski, and J Michael Rotter. A study of imperfect cylindrical steel tubes under global bending and varying support conditions. In *Proc., 8th Int. Conf. on Advances in Steel Structures, DECivil/IST/UL*, pages 22–24, 2015.

[51] V. I. Weingarten, P. Seide, and J. P. Peterson. Buckling of thin-walled circular cylinders. Technical Report NASA SP-8007, National Aeronautics and Space Administration, August 1968. URL https://ntrs.nasa.gov/archive/nasa/casi.ntrs.nasa.gov/19690013955.pdf.

[52] Randall J. Allemang. The modal assurance criterion: Twenty years of use and abuse. *Sound and Vibration*, 37(8):14–23, 2003. URL http://www.sandv.com/downloads/0308alle.pdf.

[53] Zaikun Zhang. Prima: Reference implementation for powell's methods with modernization and amelioration, 2023. URL https://doi.org/10.5281/zenodo.8052654.

[54] Marek Gryszka and Saullo G. P. Castro. Dataset for angled spar battery-wing system for large all-electric aircraft, August 2026. URL https://doi.org/10.5281/zenodo.21824981.

[55] Hussam Georges, Christian Mittelstedt, and Wilfried Becker. Rve-based grading of truss lattice cores in sandwich panels. *Archive of Applied Mechanics*, 2023. URL https://link.springer.com/article/10.1007/s00419-023-02432-1.

[56] Abdulmaliq Abiodun Alawode. Experimental analysis of wrinkling of sandwich structures. Master's thesis, University of Toulouse III Paul Sabatier, 2023. URL https://msc-frp.org/wp-content/uploads/2023/10/MSc-Thesis_2022-23_UT3-INSA_AAlawode.pdf.

[57] Mark D. Ardema, Marjorie C. Chambers, Alberto P. Patron, Andrew S. Hahn, Hiroshi Miura, and Mark D. Moore. Analytical fuselage and wing weight estimation of transport aircraft. Technical Memorandum NASA-TM-110392, National Aeronautics and Space Administration (NASA), 1996. URL https://ntrs.nasa.gov/api/citations/19960025262/downloads/19960025262.pdf.

A. Derivation of maximum von Mises Stress for the considered cross-section

One can expand the formulation of von Mises stress for beams using Equation 6:

$$\begin{aligned}\sigma_v^2 &= E^2(\bar{\epsilon} + \bar{\kappa}_y y + \bar{\kappa}_z z)^2 \\ &+3G^2[(\gamma_y - \bar{\kappa}_x z)^2 + (\gamma_z^2 + \bar{\kappa}_x y)^2]\end{aligned} \tag{18}$$

Where G is the shear modulus with shear correction applied. Then, the partial derivatives can be computed as:

$$\frac{\partial \sigma_v}{\partial y} = 2E^2(\bar{\epsilon} + \bar{\kappa}_y y + \bar{\kappa}_z z)\bar{\kappa}_y + 6G^2(\gamma_z + \bar{\kappa}_x y)\kappa_x \tag{19}$$

$$\frac{\partial \sigma_v}{\partial z} = 2E^2(\bar{\epsilon} + \bar{\kappa}_y y + \bar{\kappa}_z z)\bar{\kappa}_z - 6G^2(\gamma_y - \bar{\kappa}_x z)\kappa_x \tag{20}$$

From that, one can compute second and mixed partial derivatives and formulate the following Hessain:

$$H = \begin{bmatrix} \frac{\partial^2 \sigma_v}{\partial y^2} & \frac{\partial^2 \sigma_v}{\partial y \partial z} \\ \frac{\partial^2 \sigma_v}{\partial z \partial y} & \frac{\partial^2 \sigma_v}{\partial z^2} \end{bmatrix} \tag{21}$$

Table 10
Properties of the Goland wing [46, 48, 49]. MMOI stands for "Mass Moment Of Inertia".

Property	Value	Unit
Angle of attack	0.5	deg
Air density	1.02	kg/m^3
Chord, c_{GW}	1.8288	m
Semi-span, L	6.09	m
Max. airfoil thickness	0.04	chord
Elastic axis, x_{EA}	0.33	chord
Centre of gravity x_{CG}	0.43	chord
Mass per unit length, m/L	35.71	kg/m
MMOI at x_{EA} per unit length, $\mathcal{I}/L$	8.64	kgm
Torsional stiffness, GJ	0.99	MNm^2
Flapwise bending stiffness, EI_b	9.77	MNm^2
Chordwise bending stiffness, EI_c	0.977	GNm^2

$$H = \begin{bmatrix} 2E^2\overline{\kappa}_y^2 + 6G^2\overline{\kappa}_x^2 & 2E^2\overline{\kappa}_y\overline{\kappa}_z \\ 2E^2\overline{\kappa}_y\overline{\kappa}_z & 2E^2\overline{\kappa}_z^2 + 6G^2\overline{\kappa}_x^2 \end{bmatrix} \quad (22)$$

It is worth noting that both partial second derivatives are constant and strictly positive. This means that at the boundaries of the rectangular cross-section, there can only be local minima of von Mises stress. The determinant of the Hessian can be expressed as:

$$\det H = (2E^2\overline{\kappa}_y^2+6G^2\overline{\kappa}_x^2)(2E^2\overline{\kappa}_z^2+6G^2\overline{\kappa}_x^2)-4E^2\overline{\kappa}_y^2\overline{\kappa}_z^2 \quad (23)$$

$$\det H = 36G^2\overline{\kappa}_x^4 + 12E^2G^2\overline{\kappa}_x^2(\overline{\kappa}_y^2 + \overline{\kappa}_z^2) \quad (24)$$

This is a strictly positive expression, given that at least one of the curvatures is nonzero. Combined with the partial derivatives being positive, one can see that the function can only have local minima, which cannot correspond to the most constraining von Mises stress. As such, the critical von Mises stress must be located on the cross-section boundaries. For a rectangular cross-section, the same reasoning can be applied to the boundaries themselves, leaving the corner points as the only possible locations of the maximum von Mises stress. For a circular boundary, the second derivative along the boundary is not necessarily equal to either of the second partial derivatives in yz coordinates, so all points on the boundary remain candidates for critical points.

B. Derivation of structural to airfoil station displacement interpolation matrix

The number of structural mesh nodes is significantly larger than the number of airfoil station leading and trailing edges, which leads to information loss. The goal for the derivation of $\partial\mathbf{p}/\partial\mathbf{u}$ is to keep the model consistent in spite of this information loss while minimizing the usage of memory. To that end, it is assumed that finite element model

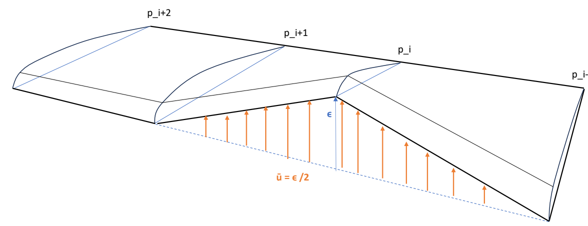

Figure 14: Deformation of the wing model in `aerosandbox` caused by deflecting a leading or trailing edge of one of the airfoils by ϵ.

displacements causing the same induced force shall cause the same $\mathbf{p}$ displacements.

The local change in angle of attack along the wing, for small displacements, is proportional to the leading and trailing edge flapwise displacements. With further assumption of 2D aerodynamic disturbances, so the local change in aerodynamic force is proportional to the local change in angle of attack, the change in aerodynamic force becomes proportional to the leading/trailing edge displacements. In `aerosandbox`, the wing is linearly interpolated between airfoil stations, so the area affected by displacement of the i-th airfoil station is the area from $(i-1)$-th to $(i+1)$-th stations:

$$p_i \propto \int_{y_{i-1}}^{y_{i+1}} u(y)dy \propto \bar{u}_{i-1}^{i+1} \quad (25)$$

This carries the additional assumption that the wing geometry does not change significantly between airfoil stations, which can lead to a large number of airfoil stations required for convergence. For wing tip airfoils, $p_{i_{\max}} \propto \bar{u}_{i_{\max}-1}^{i_{\max}}$ instead, but the following reasoning yields the same result as for inner airfoils.

The disturbances used to calculate $\partial\mathbf{F_{VLM}}/\partial\mathbf{p}$ produce a small displacement ϵ at one airfoil station. As shown in Figure 14, this leads to $\bar{u}_{i-1}^{i+1}$ or $\bar{u}_{i_{\max}-1}^{i_{\max}}$ of $\epsilon/2$ due to the linear interpolation of `aerosandbox`. Those disturbances are thus seen as generating the same change in aerodynamic force as all other disturbances with $\bar{u}$ of $\epsilon/2$.

For each station, $\bar{u}$ is estimated by sampling the displacement of the structural mesh node closest to the leading/trailing edge. Since the corresponding ϵ is $2\bar{u}$, the weight assigned to the chordwise translational degree of freedom of the sampled point in the interpolation matrix is 2, while weights assigned to all other points remain zero.

C. Verification of the aeroelastic analysis with the Goland wing benchmark

The Goland wing is an unswept rectangular wing with a parabolic airfoil and dimensions/structural properties as given in Table 10.

In order to verify the aeroelastic analysis method presented in this paper, the beam properties from the benchmark

Table 11
Comparison of Goland wing flutter speed and frequency with references.

Reference	Method	Flutter speed [m/s]	Flutter frequency [rad/s]
Goland [46]	analytical	172	67.4
Murua et al. [49]	beam + unsteady VLM (finite differences)	165 or 177	69 or 68
Palacios and Epureanu [48]	beam + 2D aero (modal)	141	69.8
Sotoudeh et al. [47]	beam + 2D aero (finite differences)	137	70.1
Present study	plate + 2D aero (finite differences)	141	69.7

are translated to an equivalent plate model. A uniform thickness plate of width $w_{pl} = 2c_{GW}/3$ and length L is created to match the elastic axis position. Plate thickness t_{pl}, elastic modulus and shear modulus are tuned to match the torsional and bending stiffness properties, and a Poisson ratio of .33 is used.

$$\begin{cases} GJ = \frac{G w_{pl} t_{pl}^3}{3} \\ EI_b = \frac{E w_{pl} t_{pl}^3}{12} \\ EI_c = \frac{E t_{pl} w_{pl}^3}{12} \end{cases} \implies \begin{cases} E = \frac{12}{w_{pl}^4}\sqrt{\frac{(EI_c)^3}{EI_b}} \\ t_{pl} = w_{pl}\sqrt{\frac{EI_b}{EI_c}} \\ G = \frac{3GJ}{w_{pl} t_{pl}^3} \end{cases} \tag{26}$$

The finite element model spanning 2/3 of the chord means that the aft-most node of the structural mesh, instead of representing the trailing edge, represents the 2/3 of the chord. This is accounted for by using 2/3 of chord length instead of its entirety when calculating the twist at airfoil stations. Similarly, for the E9X design, the wingbox width, rather than the chord length, is used to calculate airfoil station twist. Thus, the method for computing the twists is the same between this verification case and the E9X wing study case of this paper.

The density ρ_{pl} of the plate cannot be uniform, as three inertia parameters: x_{CG}, m/L and $\mathcal{I}/L$; need to be matched. Thus, it is assumed that:

$$\rho_{pl} = \mathcal{A} f_a(x) + \mathcal{B} f_b(x) + \mathcal{C} f_c(x) \tag{27}$$

where $f(x)$ are assumed functions and $\mathcal{A}$, $\mathcal{B}$ and $\mathcal{C}$ are coefficients adjusted to match the inertia parameters. ρ_{pl} is evaluated at the centre x_{cq} of each `Quad4R` element of the structural mesh. Denoting chordwise width of each element as w_q and number of elements chordwise as N_q, this leads to:

$$\begin{cases} x_{CG} = \sum^{N_q} \rho_{pl}(x_{cq}) \frac{w_q x_{cq}}{w_{pl}} \\ \frac{m}{L} = \sum^{N_q} \rho_{pl}(x_{cq}) w_q t_{pl} \\ \frac{\mathcal{I}}{L} = \sum^{N_q} \rho_{pl}(x_{cq}) w_q t_{pl} [\frac{w_q^2}{12} + (x_{cq} - x_{EA})^2] \end{cases} \tag{28}$$

Inserting Equation 27 into Equation 28 and solving for $\mathcal{A}$, $\mathcal{B}$ and $\mathcal{C}$ leads to a mass distribution that mathematically matches the inertial properties of the Goland wing. However, depending on the $f(x)$ chosen, densities of some elements might be non-positive. The set of $f(x)$ used in this study that avoids this issue was found by trial and error:

$$\begin{cases} f_a(x) = \max[0, (x - x_{CG})^5] \\ f_b(x) = \max[0, (x - x_{EA})^2] \\ f_c(x) = 1 \end{cases} \tag{29}$$

Table 12
Settings for the Goland wing aeroelastic simulation.

Parameter	Value
vortices spanwise between stations	7
vortices chordwise	10
airfoil stations	10
interpolation coefficient, n_{points}	10
natural frequencies examined	4
FEA nodes spanwise	280
FEA nodes chordwise	50

The results of the method from this study are compared against references in Table 11. With the model created, convergence has been achieved for simulation settings specified in Table 12. It can be observed that the flutter frequency does not vary significantly between the methods. The present method is closest to the results by Palacios and Epureanu [48] and stays in proximity to the other 2D aerodynamic disturbances method by Sotoudeh et al. [47]. That being said, the 2D methods collectively significantly differ from the analytical solution by Goland [46] or 3D unsteady aerodynamics by Murua et al. [49]. While the method presented in this study is verified as a correctly implemented linear aeroelastic analysis method with 2D aerodynamic disturbances, it is still subject to the limitations inherent to methods of its class. As the E9X wing is stiff and the displacements involved are small, the method is considered suitable to be used in this study, conditional on conducting a convergence study to determine the aerodynamic model resolution parameters.